

Coordinated optimization of visual cortical maps

(II) Numerical studies

Lars Reichl^{1,2,3,4,*}, Dominik Heide^{1,5}, Siegrid Löwel^{3,6}, Justin C. Crowley⁷, Matthias Kaschube⁸, Fred Wolf^{1,2,3,4*}

1 Max-Planck-Institute for Dynamics and Self-Organization, Göttingen, Germany

2 Bernstein Center for Computational Neuroscience, Göttingen, Germany

3 Bernstein Focus Neurotechnology, Göttingen, Germany

4 Faculty of Physics, Georg-August University, Göttingen, Germany

5 Frankfurt Institute of Advanced Studies, Frankfurt, Germany

6 School of Biology, Georg-August University, Göttingen, Germany

7 Carnegie Mellon University, Department of Biological Sciences, Pittsburgh PA, USA

8 Physics Department and Lewis-Sigler Institute, Princeton University, Princeton NJ, USA

* E-mail: reichl@nld.ds.mpg.de; fred@nld.ds.mpg.de

Abstract

It is an attractive hypothesis that the spatial structure of visual cortical architecture can be explained by the coordinated optimization of multiple visual cortical maps representing orientation preference (OP), ocular dominance (OD), spatial frequency, or direction preference. In part (I) of this study we defined a class of analytically tractable coordinated optimization models and solved representative examples in which a spatially complex organization of the orientation preference map is induced by inter-map interactions. We found that attractor solutions near symmetry breaking threshold predict a highly ordered map layout and require a substantial OD bias for OP pinwheel stabilization. Here we examine in numerical simulations whether such models exhibit biologically more realistic spatially irregular solutions at a finite distance from threshold and when transients towards attractor states are considered. We also examine whether model behavior qualitatively changes when the spatial periodicities of the two maps are detuned and when considering more than 2 feature dimensions. We show that, although maps typically undergo substantial rearrangement, no other solutions than pinwheel crystals and stripes dominate in the emerging layouts. Moreover, pinwheel crystallization takes place on a rather short timescale and can

also occur for detuned wavelengths of different maps. Increasing the number of feature maps changes conditions for pinwheel stabilization. In higher dimensional models we find that that stabilization by crystallization can be achieved even without an OD bias. Our numerical results thus support the view that neither minimal energy states nor intermediate transient states of our coordinated optimization models successfully explain the spatially irregular architecture of the visual cortex. We discuss several alternative scenarios and additional factors that may improve the agreement between model solutions and biological observations.

Author Summary

Neurons in the visual cortex of carnivores, primates and their close relatives form spatial representations or maps of multiple stimulus features. In part (I) of this study we theoretically predicted maps that are optima of a variety of optimization principles. When analyzing the joint optimization of two interacting maps we showed that for different optimization principles the resulting optima show a stereotyped, spatially perfectly periodic layout. Experimental maps, however, are much more irregular. In particular, in case of orientation columns it was found that different species show an apparently species invariant statistics of point defects, so-called pinwheels. In this paper, we numerically investigate whether the spatial features of the stereotyped optima described in part (I) are expressed on a biologically relevant timescale and whether other, spatially irregular, long-living states emerge that better reproduce the experimentally observed statistical properties of orientation maps. Moreover, we explore whether the coordinated optimization of more than two maps can lead to spatially irregular optima.

Introduction

In the primary visual cortex of primates and carnivores, functional architecture can be characterized by maps of various stimulus features such as orientation preference (OP), ocular dominance (OD), spatial frequency, or direction preference [1–21]. Many attempts have been made to explain and understand the spatial organization of these maps as optima of specific energy functionals the brain minimizes either during development or on evolutionary timescales [22–38]. In part (I) of this study we presented an analytical approach to study the coordinated optimization of interacting pairs of visual cortical maps

where maps are described by real and complex valued order parameter fields [39]. We used symmetry considerations to derive a classification and parametrization of conceivable inter-map coupling energies and identified a representative set of inter-map coupling terms: a gradient-type and a product-type coupling energy which both can enter with different power in the dynamics. Examining this set of inter-map coupling energies was further motivated by the experimentally observed geometric relationships between cortical maps [5, 7, 15, 19, 26, 40, 41]. We examined the impact of these coupling energies in a system of coupled Swift-Hohenberg equations which without coupling lead to regular stripe patterns in the complex valued order parameter field. Our analytical results demonstrated that various types of inter-map coupling energies can induce the formation of defect structures, so-called pinwheels, in the complex order parameter field describing the OP map. For solutions that can become optima of the model, pinwheels are arranged on regular periodic lattices such as rhombic pinwheel crystals (rPWCs) or hexagonal pinwheel crystals (hPWCs). Our analysis focused on the optimization of a single pair of feature maps where the complex valued map represents the OP map and the real map represents the OD map. For this case we presented a complete characterization of the stable OP and OD patterns, stripe-like solutions, rhombic and hexagonal crystal patterns predicted by the coordinated optimization models. In all analyzed models pinwheel crystallization was conditional on a substantial bias in the response properties of the co-evolving real-valued map.

The pinwheel crystals we obtained, although beautiful and easy to characterize, strongly deviate from the spatially irregular design observed for OP maps in the visual cortex [2–4]. A large scale empirical study of the arrangement of pinwheel positions and their spatial densities in the visual cortex of three species widely separated in mammalian evolution recently showed that orientation maps although spatially irregular precisely conform with apparently species insensitive quantitative layout rules [42]. In particular, it was found that not only the mean density of pinwheels but also number fluctuations over a wide range of spatial scales and local next neighbor arrangements within individual hypercolumns agree in their statistical features across species with an accuracy in the range of a few percent [42]. In contrast to the large variability of local map layouts in experimentally observed maps [1–21], the pinwheel crystals found in the coordinated optimization models introduced in part (I) show a regular and stereotyped structure. Quantitatively, all PWC solutions that we found exhibit a large pinwheel density of about 3.5 or even 5.2 pinwheels per hypercolumn. In contrast, for experimental OP maps the average pinwheel density was found to be statistical indistinguishable from the mathematical constant π up to a precision of 2% [42–44].

Our previous analytical results on optima thus raise the question how coordinated optimization of OP and OD maps can be reconciled with the experimentally observed layout rules of orientation maps.

From a general perspective, one might suspect that the crystalline layout of local minima and optima results from the restrictions of the applied perturbation method which allowed us to study optima analytically. Furthermore, results might be expected to change substantially if one would consider the coordinated optimization of more than two feature maps. Examining this aspect is demanded because of the presence of multiple feature maps in the visual cortex of primates and carnivores and by the general expectation that geometrical rules coordinating map layout might be the harder to satisfy the more maps are simultaneously optimized. Finally, when studying optima of a particular optimization principle we disregarded transient states that could in principle dominate developmental optimization on biologically relevant timescales and are expected to be more irregular. Analytical results were obtained using a perturbative treatment close to the pattern forming threshold. This perturbative treatment, however, gives no information on the speed with which singularities that were initially generated during spontaneous symmetry breaking will crystallize into highly ordered arrays. It is conceivable that this process may occur on very long timescales. If this was the case, developmental optimization may lead to long-lived spatially irregular states that are transients towards regular patterns that would be reached after very long times or potentially never.

In part (I) we showed that one can neglect the backreaction of the OP map onto the OD map if the OD map is 'dominant' i.e. their amplitudes are much larger than those of the OP map. This can be achieved for a sufficiently small ratio of their distances to threshold. This finding raises questions that cannot be addressed purely perturbatively. Do the observed local minima and optima of the analyzed optimization principles persist when taking the backreaction into account or when considering map formation further from the pattern formation threshold? Besides the influence of the backreaction the full dynamical system receives additional corrections. There are higher order corrections to the uncoupled amplitude equations which can become important for finite bifurcation parameters neglected in [39]. In part (I) of this study we also assumed equal periodicities of the two interacting maps. Experiments suggest that the different periodicities in the layout of OP and OD maps can have an impact on the map layout [7, 45, 46]. It is thus also interesting to explore whether and how a detuning of typical periodicities affects optimal layouts and whether it can lead to spatially irregular maps.

To assess these issues we generalized the field dynamics to describe the coordinated optimization of cou-

pled complex valued and several real valued scalar fields. From a practical point of view, the analyzed phase diagrams and pattern properties indicate that the higher order gradient-type coupling energy is the simplest and most convenient choice for constructing models that reflect the correlations of map layouts in the visual cortex. For this coupling, intersection angle statistics are reproduced well, pinwheels can be stabilized, and pattern collapse cannot occur. In this study we thus numerically analyzed the dynamics of coordinated optimization focussing on the high order gradient-type inter-map coupling energy. We use a fully implicit integrator based on the Crank-Nicolson scheme and a Newton-Krylow solver. In numerical simulations we characterize the kinetics and conditions for pinwheel crystallization and the creation of pinwheels from a pinwheel-free initial pattern. The latter is a sufficient but not necessary criterion for systems in which a pinwheel-rich state corresponds to an energetically favored state. As we point out this criterion can be easily assessed in models of arbitrary complexity that otherwise evade analytical treatment. We further explored the impact of inter-map wavelength differences, as observed in certain species, on the structure of the resulting solutions. Finally, we extended the presented models to explore the coordinated optimization of more than two feature maps. To examine whether the observed quantitative properties can be reproduced in models for the coordinated optimization of maps we calculated various pinwheel statistics during optimization. We find that spatially irregular patterns decay relatively fast into locally crystalline arrays. Further long-term rearrangement mainly leads to the emergence of long-range spatial alignment of local crystalline arrangements. We showed that the previous finding that OD stripes are not able to stabilize pinwheels generalizes to the case of detuned wavelengths. The observation that the coordinated optimization of two interacting maps leads to spatially perfectly periodic optima is also robust to detuned typical wavelengths and to the inclusion of more than two feature maps. Our results suggest that the coordinated optimization of multiple maps that would in isolation exhibit spatially perfectly periodic optimal layouts on its own cannot explain the experimentally observed spatially irregular design of OP maps in the visual cortex and its quantitative aspects. We consider alternative scenarios and propose ways to incorporate inter-map relations and joint optimization in models in which the optimal OP map layout is intrinsically irregular already for vanishing inter-map coupling.

Results

1.1 A dynamical systems approach

We model the response properties of neuronal populations in the visual cortex by two-dimensional scalar order parameter fields which are either complex valued or real valued [47–49]. We consider inter-map coupling between a complex valued map $z(\mathbf{x})$ and one or several real valued maps $o_i(\mathbf{x})$. The complex valued field $z(\mathbf{x})$ can for instance describe OP or direction preference of a neuron located at position \mathbf{x} . A real valued field $o(\mathbf{x})$ can describe for instance OD or the spatial frequency preference. Although we consider a model for the coordinated optimization of general real and complex valued order parameter fields we view $z(\mathbf{x})$ as the field of OP throughout this article to aid comparison to the biologically observed patterns. In this case, the pattern of preferred stimulus orientation ϑ is obtained by

$$\vartheta(\mathbf{x}) = \frac{1}{2} \arg(z). \quad (1)$$

The modulus $|z(\mathbf{x})|$ is a measure of orientation selectivity at cortical location \mathbf{x} .

OP maps are characterized by so-called *pinwheels*, regions in which columns preferring all possible orientations are organized around a common center in a radial fashion [47, 50–52]. The centers of pinwheels are point discontinuities of the field $\vartheta(\mathbf{x})$ where the mean orientation preference of nearby columns changes by 90 degrees. Pinwheels can be characterized by a topological charge q which indicates in particular whether the orientation preference increases clockwise or counterclockwise around the pinwheel center,

$$q_i = \frac{1}{2\pi} \oint_{C_i} \nabla \vartheta(\mathbf{x}) ds, \quad (2)$$

where C_i is a closed curve around a single pinwheel center at \mathbf{x}_i . Since ϑ is a cyclic variable in the interval $[0, \pi]$ and up to isolated points is a continuous function of \mathbf{x} , q_i can only have values

$$q_i = \frac{n}{2}, \quad (3)$$

where n is an integer number [53]. If its absolute value $|q_i| = 1/2$, each orientation is represented only once in the vicinity of a pinwheel center. In experiments, only pinwheels with a topological charge of $\pm 1/2$ have been observed, which are simple zeros of the field $z(\mathbf{x})$.

In case of a single real valued map $o(\mathbf{x})$ the field can be considered as the field of OD, where $o(\mathbf{x}) < 0$ indicates ipsilateral eye dominance and $o(\mathbf{x}) > 0$ contralateral eye dominance of the neuron located at position \mathbf{x} . The magnitude indicates the strength of the eye dominance and thus the zeros of the field corresponding to the borders of OD.

As visual cortical maps are described by optima of an energy functional E , a formal time evolution of these maps that represents the the gradient descent of this energy functional can be used to obtain predicted map layouts. The field dynamics thus takes the form

$$\begin{aligned}\partial_t z(\mathbf{x}, t) &= F[z(\mathbf{x}, t), o_1(\mathbf{x}, t), o_2(\mathbf{x}, t), \dots] \\ \partial_t o_i(\mathbf{x}, t) &= G_i[z(\mathbf{x}, t), o_1(\mathbf{x}, t), o_2(\mathbf{x}, t), \dots],\end{aligned}\tag{4}$$

where $F[z, o_i]$ and $G_i[z, o_i]$ are nonlinear operators given by $F[z, o_i] = -\frac{\delta E}{\delta z}$, $G_i[z, o_i] = -\frac{\delta E}{\delta o_i}$. The system then relaxes towards the minima of the energy E . The convergence of this dynamics towards an attractor is assumed to represent the process of maturation and optimization of the cortical circuitry. Various biologically detailed models can be cast into the form of Eq. (4) [22, 49, 54].

To dissect the impact of inter-map coupling interactions we split the energy functional E into single field and interaction components $E = E_z + E_{o_i} + \sum_i U_{zo}(z, o_i) + \sum_{i \neq j} U_{oo}(o_i, o_j)$. All visual cortical maps are arranged in roughly repetitive patterns of a typical wavelength Λ that may be different for different maps. We chose E_z to obtain, in the absence of coupling, a well studied model reproducing the emergence of a typical wavelength by a pattern forming instability, the Swift-Hohenberg model [55, 56]. This model has been characterized comprehensively in the pattern formation literature and mimics the behavior of for instance the continuous Elastic Network or the Kohonen model for orientation selectivity (see [22]). We note that many other pattern forming systems occurring in different physical, chemical, and biological contexts (see for instance [57–60]) have been cast into a dynamics of the same form. Its dynamics in case of the OP map is of the form

$$\partial_t z(\mathbf{x}, t) = \hat{L}z(\mathbf{x}, t) - |z|^2 z,\tag{5}$$

with the linear Swift-Hohenberg operator

$$\hat{L} = r - (k_c^2 + \Delta)^2,\tag{6}$$

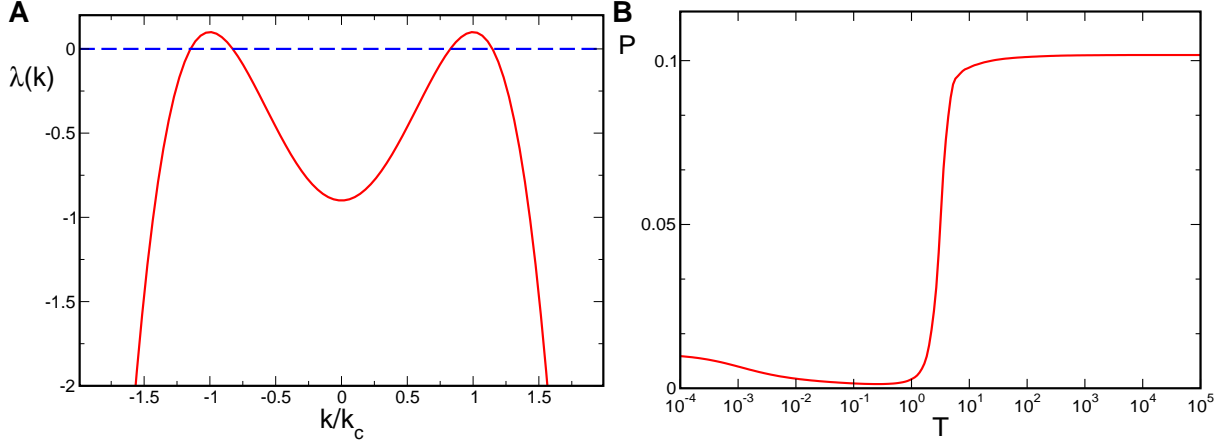


Figure 1. Swift-Hohenberg equation, A Cross section through the spectrum $\lambda(k)$ of the Swift-Hohenberg operator Eq. (7), $r = 0.1$. **B** Time evolution of the Power, Eq. (8), for spatial white noise initial conditions.

$k_c = 2\pi/\Lambda$, and Δ the Laplace operator. In Fourier representation, \hat{L} is diagonal with the spectrum

$$\lambda(k) = r - (k_c^2 - k^2)^2. \quad (7)$$

The spectrum exhibits a maximum at $k = k_c$, see Fig. 1(a). For $r < 0$, all modes are damped since $\lambda(k) < 0, \forall k$ and only the homogeneous state $z(\mathbf{x}) = 0$ is stable. This is no longer the case for $r > 0$ when modes on the *critical circle* $k = k_c$ acquire a positive growth rate and grow, resulting in patterns with a typical wavelength $\Lambda = 2\pi/k_c$. This model exhibits a supercritical bifurcation where the homogeneous state loses its stability and spatial pattern emerge.

While the linear part of the dynamics establishes a typical wavelength, the nonlinear term in the dynamics leads to the selection of the final pattern. In this study we measure time $T = rt$ in units of the intrinsic timescale which is associated with the growth rate of the linear part Eq. (6). Considering the time evolution of Eq. (5) initialized with a random OP map and low selectivity (small $|z|$) several different stages of the dynamics can be distinguished. The linear part forces modes on the critical circle to grow with rate r while strongly suppressing modes off the critical circle when starting from small amplitude white noise initial conditions, see Fig. 1A. The OP map becomes more ordered in this linear phase as one dominant wavelength emerges. The total power of the field is given by

$$P(t) = \langle |z(\mathbf{x}, t)|^2 \rangle_{\mathbf{x}}, \quad (8)$$

where $\langle \rangle_{\mathbf{x}}$ denotes spatial average. The time dependence of the power reflects the different growth rates among modes. The time evolution of the power is depicted in Fig. 1B. Initially, the power decreases slightly due to the suppression of modes outside the circle of positive growth rate. At $T \approx 1$ there is a rapid increase and then a saturation of the power. The amplitudes of the Fourier modes reach their stationary values and $P \propto r$. At this stage of the evolution the influence of the nonlinear part becomes comparable to that of the linear part. Once the modes saturate the phase of nonlinear competition between the active modes along with a reorganization of the structure of the OP map starts. The competition between active modes leads to pattern selection. The final pattern then consists of distinct modes in Fourier space [56, 61]. Once the active modes are selected a relaxation of their phases takes place.

Inter-map coupling can influence the time evolution on all stages of the development depending on whether this coupling affects only the nonlinear part or also the linear one. When incorporating additional maps into the system in all cases we rescaled the dynamics by the bifurcation parameter of the OP map i.e. $T = r_z t$. The coupled dynamics we considered is of the form

$$\begin{aligned}\partial_t z(\mathbf{x}, t) &= \hat{L}_z z(\mathbf{x}, t) - |z|^2 z - \frac{\delta U}{\delta \bar{z}} \\ \partial_t o_i(\mathbf{x}, t) &= \hat{L}_{o_i} o_i(\mathbf{x}, t) - o_i^3 - \frac{\delta U}{\delta o_i} + \gamma,\end{aligned}\tag{9}$$

where $\hat{L}_{\{o_i, z\}} = r_{\{o_i, z\}} - \left(k_{c, \{o_i, z\}}^2 + \Delta\right)^2$, and γ is a constant. To account for the differences in the dominant wavelengths of the patterns we chose two typical wavelengths $\Lambda_z = 2\pi/k_{c, z}$ and $\Lambda_{o_i} = 2\pi/k_{c, o_i}$. Since in cat visual cortex the typical wavelength for OD and OP maps are approximately the same [45, 46] i.e. $k_{c, o} = k_{c, z} = k_c$ the Fourier components of the emerging pattern in this case are located on a common critical circle, see however [62]. The dynamics of $z(\mathbf{x}, t)$ and $o_i(\mathbf{x}, t)$ are coupled by interaction terms which can be derived from a coupling energy U . Many optimization models of the form presented in Eq. (4) have been studied [22–38]. The concrete dynamics in Eq. (9) is the simplest which in the uncoupled case leads to pinwheel-free OP stripe patterns and to a stripe-like or patchy layout of the co-evolving real valued fields.

As revealed by the symmetry-based classification of coupling energies

$$U = \alpha o^2 |z|^2 + \beta |\nabla z \cdot \nabla o|^2 + \tau o^4 |z|^4 + \epsilon |\nabla z \cdot \nabla o|^4,\tag{10}$$

parametrizes a representative family of biologically plausible coupling energies for a single real valued map o , see part (I), [39].

The numerical integration scheme to solve Eq. (9) is detailed in the Methods part. Initial conditions for the OD map were chosen as stripe, hexagonal, or constant patterns plus Gaussian white noise. Initial conditions for the OP map are either pinwheel-free OP stripes or band-pass filtered Gaussian white noise for which the average pinwheel density is bounded from below by the constant π [22]. For numerical analysis we focused on the high order gradient-type inter-map coupling energy. This energy can reproduce all qualitative relationships found between OP and OD maps, does not suffer from potential OP map suppression, and leads to a relatively simple phase diagram for two interacting maps near threshold.

1.2 Final states

In part (I) we calculated phase diagrams for different inter-map coupling energies [39]. In all cases, hexagonal PWCs can be stabilized only in case of OD hexagons. We tested these results numerically. Numerical simulations of the dynamics Eq. (9) with the coupling energy

$$U = \epsilon |\nabla z \cdot \nabla o|^4, \quad (11)$$

are shown in Fig. 2. All remaining inter-map coupling energies in Eq. (10) are assumed to be zero. The initial conditions and final states are shown for different bias terms γ and inter-map coupling strengths ϵ . Note the logarithmic time scales. Pinwheel densities rapidly diverge from values near 3.1 as soon as the map exhibits substantial power $1 < T < 10$. We observed that for a substantial contralateral bias and above a critical inter-map coupling pinwheels are preserved for all times or are generated if the initial condition is pinwheel-free. Without a contralateral bias the final states were pinwheel-free stripe solutions irrespective of the strength of the inter-map coupling.

1.3 Kinetics of pinwheel crystallization

To characterize the process of pinwheel annihilation, preservation, and creation during progressive map optimization we calculated the pinwheel density as well as various other pinwheel statistics (see Methods) during the convergence of patterns to attractor states. The time evolution of the pinwheel density is shown

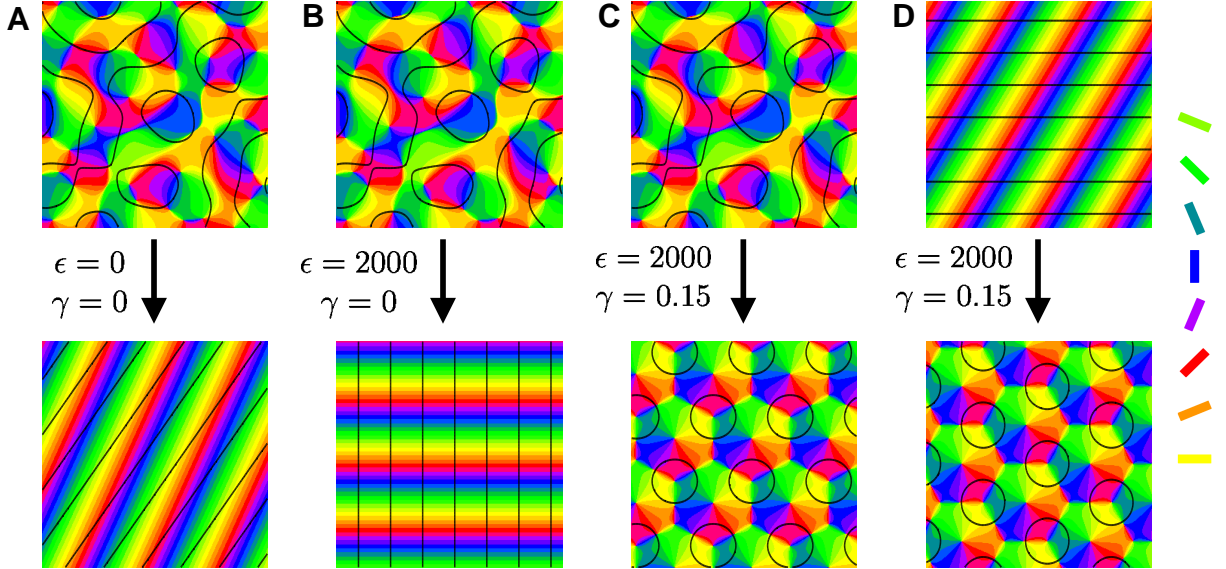


Figure 2. Pinwheel annihilation, preservation, and generation in numerical simulations for different strengths of inter-map coupling ϵ and OD bias γ . Color code of OP map with zero contours of OD map superimposed. **A** $\gamma = 0, \epsilon = 0$ **B** $\gamma = 0, \epsilon = 2000$ **C** and **D** $\gamma = 0.15, \epsilon = 2000$. Initial conditions identical in **A** - **C**, $r_o = 0.2, r_z = 0.02, T_f = 10^4, k_{c,o} = k_{c,z}$.

in Fig. 3. In the uncoupled case ($\epsilon = 0$) most of the patterns decayed into a stripe solution and their pinwheel density dropped to a value near zero. At small coupling strengths ($\epsilon = 200$) the pinwheel density converged either to zero (stripes), to values near 3.5 for the rPWC (see part (I), Figure S6), or to approximately 5.2 for the contra-center hPWC (see part (I), Figure S7). At high inter-map coupling ($\epsilon = 2000$) pinwheel free stripe patterns formed neither from pinwheel rich nor from pinwheel free initial conditions. In this regime the dominant layout was the contra-center hPWC. When starting from OD and OP stripes, see Fig. 3C (green lines), the random orientation between the stripes first evolved towards a perpendicular orientation ($T \approx 1$). This led to a transient increase in the pinwheel density. At the time ($T \approx 10$) where the OD stripes dissolve towards OD hexagons hPWC solutions formed and the pinwheel density reached its final value.

Regions of hPWC layout can however be inter-digited with long lived rPWC solutions and stripe domains. Figure 3D shows the time course of the normalized power $P_n(t) = \langle |z(\mathbf{x}, t)_{\text{dyn}}|^2 \rangle_{\mathbf{x}} / \langle |z(\mathbf{x}, t)_{\text{th}}|^2 \rangle_{\mathbf{x}}$, where $\langle \rangle_{\mathbf{x}}$ denotes spatial average. The field z_{th} is obtained from the solution of the amplitude equations (see [39]) while z_{dyn} is the field obtained from the simulations. Starting from a small but nonzero power the amplitudes grew and saturated after $T \approx 1$. When the amplitudes were saturated the selection of the

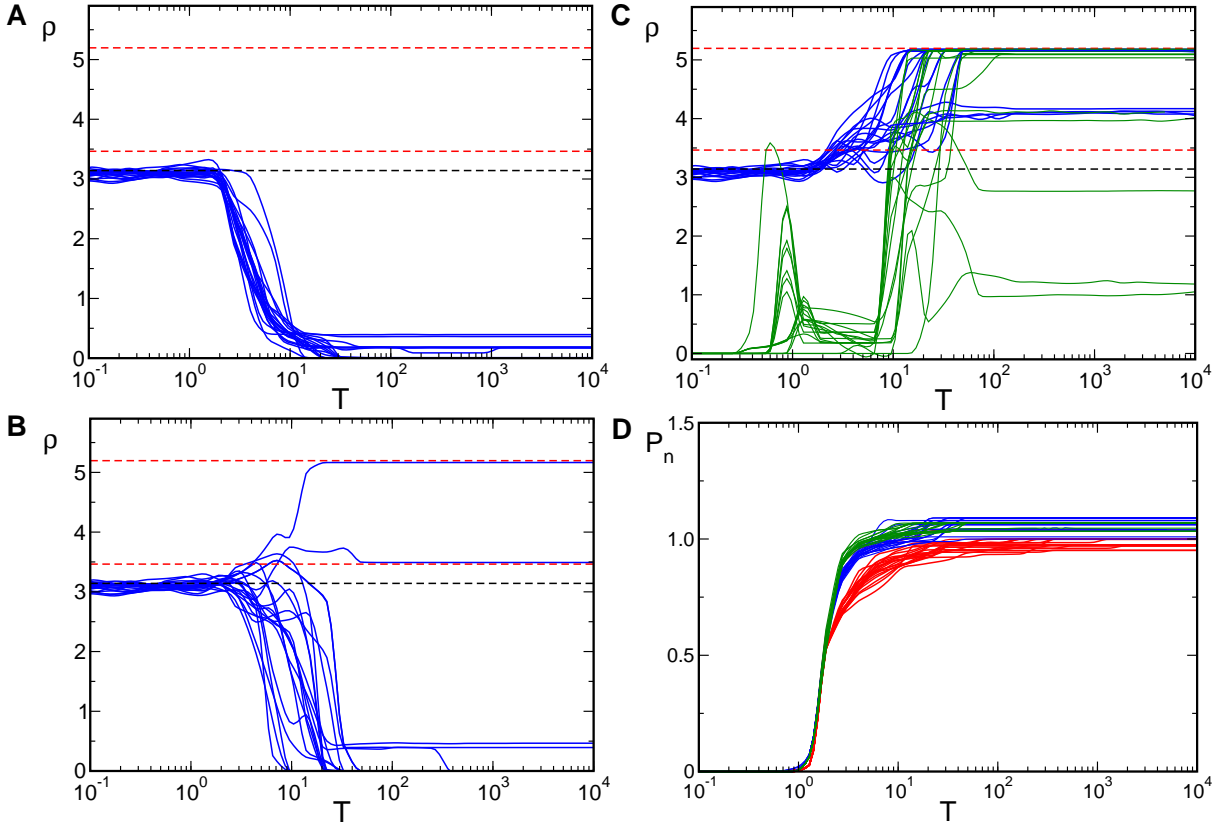


Figure 3. Time evolution of the pinwheel density, $U = \epsilon |\nabla z \cdot \nabla o|^4$, $r_z = 0.05$, $r_o = 0.25$, $\gamma = 0.15$. For each parameter set **A-C** simulations in blue started from an identical set of 20 initial conditions. Red dashed lines: $\rho = 4 \cos(\pi/6)$ and $\rho = 6 \cos(\pi/6)$, black dashed line: $\rho = \pi$. **A** $\epsilon = 0$ **B** $\epsilon = 200$ **C** $\epsilon = 2000$. **D** Normalized power of OP map, $\epsilon = 0$ (red), $\epsilon = 200$ (blue), and $\epsilon = 2000$ (green). In green **C**: OD and OP stripes as initial conditions. Parameters: 128×128 mesh, $\Gamma = 22$.

final pattern started. Quantitatively, we found that with weak backreaction the critical coupling strengths were slightly increased compared to their values in the limit $r_z \ll r_o$. Snapshots of the simulation leading to the hPWC solutions at three time frames are shown in Fig. ???. Already at $T \approx 0.8$ a substantial rearrangement of the pattern took place and one can identify different domains in the pattern that are locally highly stereotyped.

For the time evolution of the maps we also calculated the distributions of pinwheel next-neighbor distances d , measured in units of the column spacing Λ . The distributions of distances for simulations leading to rhombic and hPWC solutions are shown in Fig. 5. They are characterized by three stages in the evolution of the pinwheel distances. At early stages of the evolution ($10^{-2} \leq T$) there is a continuous distribution starting approximately linearly from $d = 0$. At the time where the amplitudes saturated ($T \approx 1$)

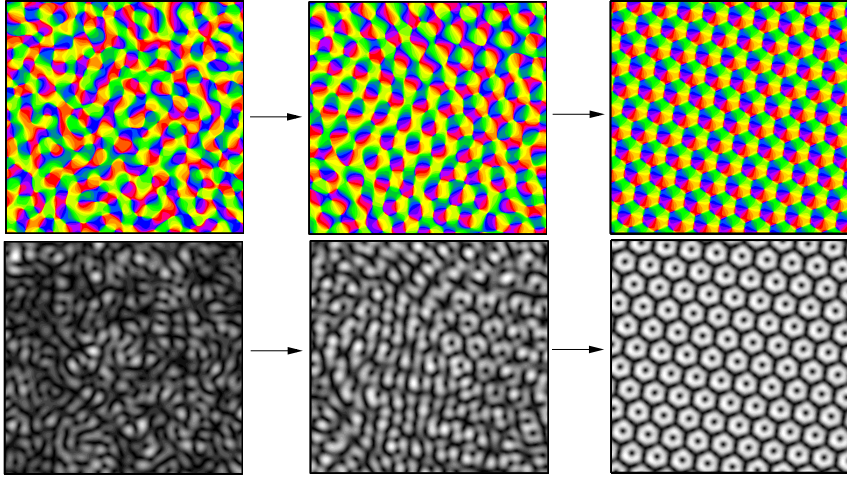


Figure 4. Snapshots of the pinwheel crystallization process. Top panel: OP map, bottom panel: selectivity $|z(\mathbf{x})|$. Left: $T = 0.01$, middle: $T = 0.8$, right: $T = T_f = 10^4$. Parameters as in Fig. 3(c), $\epsilon = 2000$, $\gamma = 0.15$

the distribution of pinwheel distances became very inhomogeneous. Different domains with stripe-like, rhombic, or hexagonal patterns appeared (see also Fig. 7C,D) until for $T > 10$ the rhombic or hexagonal pattern took over the entire pattern.

As pinwheels carry a topological charge we could divide the distributions according to distances between pinwheels of the same charge or according to distances between pinwheels of the opposite charge. In Fig. 6 we present pinwheel distances for the final states of the dynamics. In case of the rhombic solutions there is only a single pinwheel to pinwheel distance with $d = 1/\sqrt{3}\Lambda \approx 0.58\Lambda$. In numerical simulations small variations in the amplitudes lead to a slightly larger distance between pinwheels of equal charge than between pinwheels of opposite charge. Therefore their distance distributions do not collapse exactly, see Fig. 6A. In case of the hPWC there are three peaks at $d \approx 0.28\Lambda$, $d \approx 0.36\Lambda$ and $d \approx 0.56\Lambda$ in the pinwheel distance distribution of arbitrary charge, see Fig. 6B. These three peaks all result from distances between pinwheels carrying the opposite charge while the distance between pinwheels of the same charge shows two peaks at $d \approx 0.48\Lambda$ and $d \approx 0.64\Lambda$ in the distribution. The origin of the peaks is indicated in Fig. 6C and Fig. 6D.

These results confirm that inter-map coupling can induce the stabilization of pinwheels in the OP pattern. This however does not mean that the pinwheels initially generated by spontaneous symmetry breaking will be preserved during convergence of the map. To what extent are the pinwheels in the crystalline OP maps preserved from pinwheels of the initial OP pattern? To answer this question we calculated

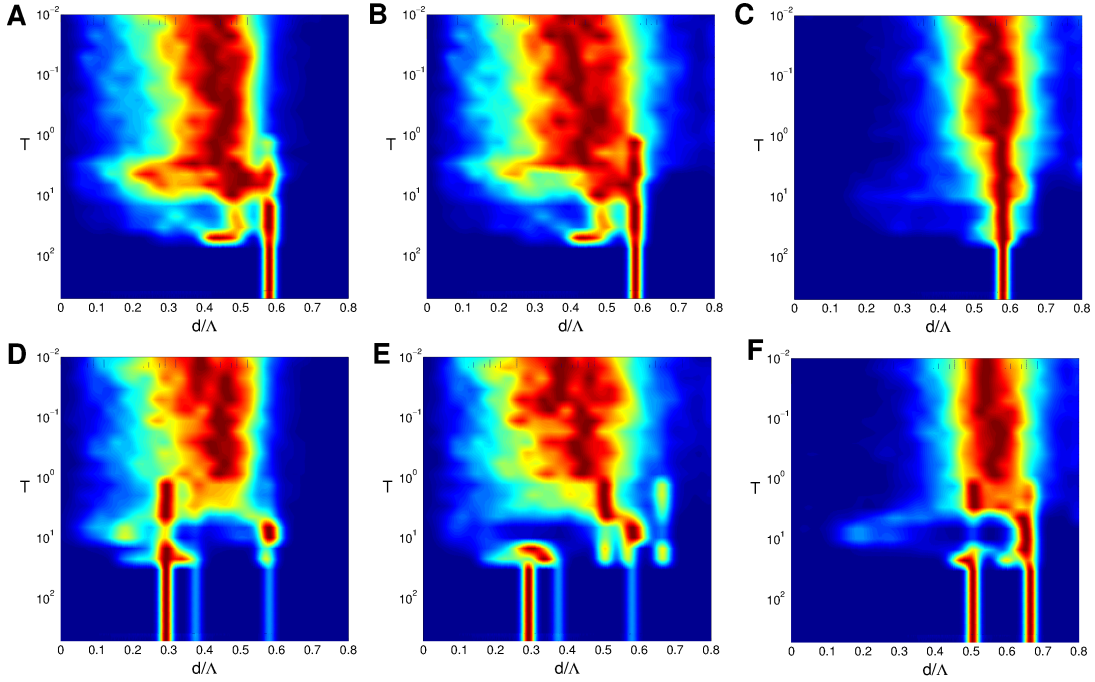


Figure 5. Distribution of nearest neighbor pinwheel distances during development. A-C rPWC **D-F** hPWC. Distance to the next pinwheel of arbitrary **A,D**, opposite **B,E**, and equal **C,F** topological charge. Parameters as in Fig. 3B.

the pinwheel annihilation $a(t)$ and creation $c(t)$ rate during time evolution, see Methods. The time evolution of these rates, averaged over 20 simulations leading to a hPWC, is shown in Fig. 7A. We observe that both rates were fairly similar throughout development, with a slightly higher creation rate in the later stage of development. During the initial stages of time evolution creation and annihilation rates decay algebraically $c, a \propto 1/T$. At $T \approx 3$ both rates deviate from this algebraic decay. From thereon annihilation and creation rates increase, reflecting the nonlinear rearrangement of the pattern. After $T \approx 15$ no pinwheels are created or annihilated anymore and the pinwheels of the final pattern are present.

Pinwheels are created and annihilated until a first crystal-like pattern is formed. How many pinwheels of the initial pattern are still present in the final pattern? For a given set of pinwheels at an initial time $T = T^*$ we further calculate the fraction $s(t)$ of those pinwheels surviving until time T . The fraction of pinwheels present at time T^* that survive up to the final time $T = T_f$ is given by $p(t)$. Both fractions are shown in Fig. 7B for $T^* = 0.01$ and in Fig. 7C for $T^* = 2$, a time where the power $P(t)$ has almost

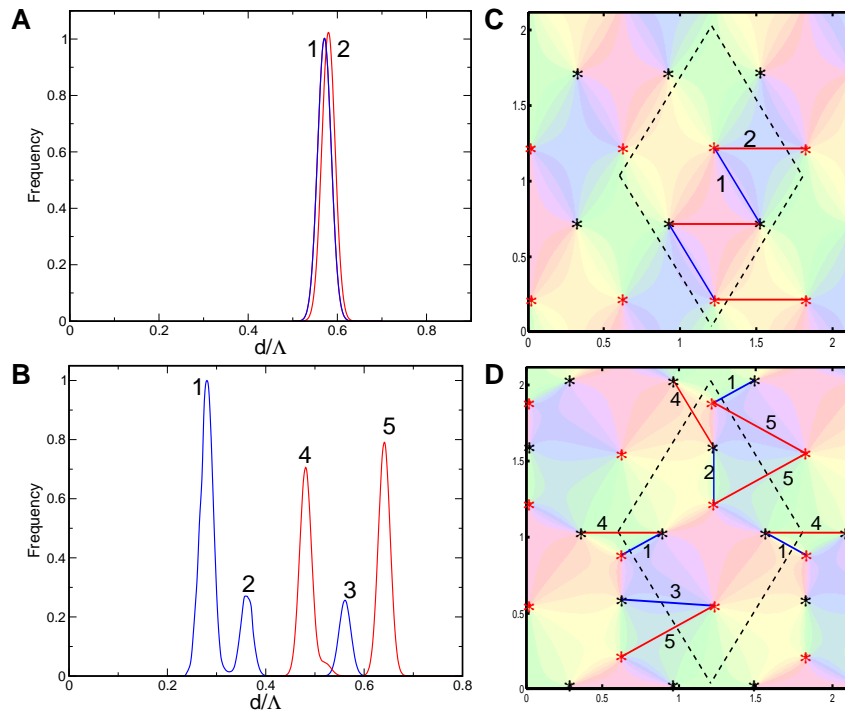


Figure 6. Distribution of nearest neighbor distances for final states ($T = T_f = 10^4$). **A** rPWC, **B** hPWC with pinwheels of equal (red) and opposite (blue) charge. **C** and **D** Illustration of occurring pinwheel distances. Pinwheels are marked with star symbols according to their charge. Units are given in Λ . Parameters as in Fig. 3B.

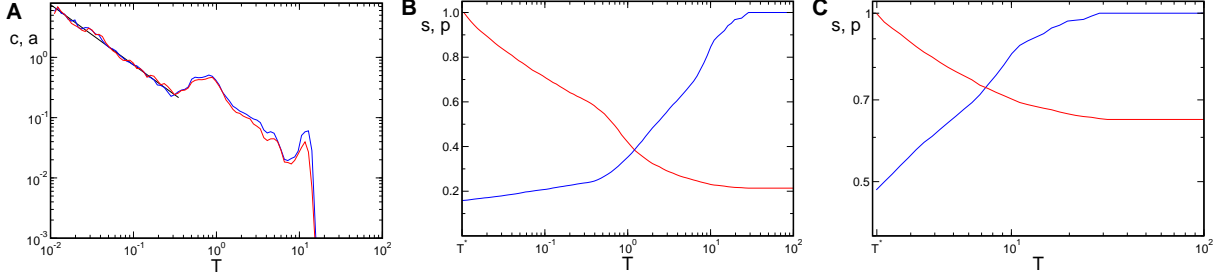


Figure 7. Pinwheel annihilation and creation. **A** Creation (blue) and annihilation (red) rates during time evolution. Fit: $c, a = 0.08/T$ (black line). **B,C** Survival fraction (red) and fraction of preserved pinwheels (blue) compared to the initial time $T^* = 0.01$ **B** and $T^* = 2$ **C**. Parameters as in Fig. 3C.

saturated, see Fig. 3D. We observed that about 20% of the initial pinwheels are preserved until the final time and therefore most of the pinwheels of the crystal pattern are created during development. From those pinwheels which are present when the power saturates about 65% are also present in the final pattern.

1.4 Detuning OD and OP wavelengths: OD stripes

The analytical results obtained in [39] as well as the previous numerical results (see Fig. 2B) predict that OD stripes do not lead to spatially complex patterns and are not capable of stabilizing pinwheels. In case of gradient-type inter-map couplings the OP map consists of stripes which run perpendicular to the OD stripes. In case of the product-type inter-map coupling high gradient regions of both maps avoid each other by producing again OP stripes but now running in the same direction as the OD stripes. In numerical simulations we also investigated the case of OD stripes of larger wavelength than OP columns, as is the case in macaque monkey primary visual cortex [7, 63]. In case of a gradient-type inter-map coupling we find that the OD bands are perpendicular to the OP bands independent of the ratio $\Lambda_o/\Lambda_z > 1$, see Fig. 8C,D. In case of the product-type inter-map coupling, if the ratio $\Lambda_o/\Lambda_z > 1$, orientation representation does not collapse as it would be the case for $\Lambda_o = \Lambda_z$, see [39]. The system, however, again finds a way to put zero contours ($\text{Re } z = 0$ and $\text{Im } z = 0$) along the OD maximum which now is a fracture line, see Fig. 8E,F. The angle between the active OP and OD modes is given by $\alpha = \arccos k_{c,o}/k_{c,z}$ corresponding to the resonance condition $\vec{k}_{1,z} - \vec{k}_{2,z} - 2\vec{k}_{1,o} = 0$, see Fig. 8A.

1.5 Detuning OD and OP wavelengths: OD hexagons

In case of identical wavelengths $k_{c,o} = k_{c,z}$ strong interaction with a system of hexagonal OD patches leads to hPWC solutions. For these solutions pinwheel positions are correlated with OD extrema. For instance in case of the higher order gradient-type inter-map coupling energy, for which the contra-center PWC corresponds to the energetic ground state, half of the pinwheels are located at OD extrema while the remaining half is located near OD borders, see Figure S7 of part (I) [39]. If, however, the typical wavelengths of OD and OP patterns are not identical such a precise relationship cannot be fulfilled in general. We therefore studied whether a detuning of typical wavelengths can lead to spatially irregular and pinwheel rich OP patterns. In numerical simulations which lead to OD hexagons with a fixed wavelength we varied the OP wavelength using identical initial conditions. Wavelength ratios are chosen such that each pattern exhibited an integer aspect ratio. Wavelength ratios were $\Lambda_o/\Lambda_z = n/41$ with n an integer. Examples of final patterns of such simulations are shown in Fig. 9 using the high order gradient-type inter-map coupling energy. In all studied cases the final patterns are spatially regular. The observed patterns are either fractured stripe patterns with two active modes Fig. **9A,C,D,E** or rPWC (two modes plus the corresponding opposite modes), see Fig. **9B,F**. For a large ratio $k_{c,o}/k_{c,z}$ the patterns with two active modes are pinwheel free, see Fig. **9A,C,D**. For smaller ratios $k_{c,o}/k_{c,z}$ the patterns are pinwheel rich, see Fig. **9E**. The pinwheel density appears to exhibit a complex dependence on the wavelength ratio since solutions switch back and forth between pinwheel-free fracture stripes and pinwheel-rich rPWCs when the wavelength ratio is decreased from 1. Much larger domains than used in the current simulations would be needed to simulate values intermediate to the wavelength ratios used here. Our results, nevertheless, clearly establish that OD induced pinwheel stabilization can occur also with detuned wavelengths. They furthermore confirm that wavelength detuning does not by itself generates irregular stable maps in the considered model.

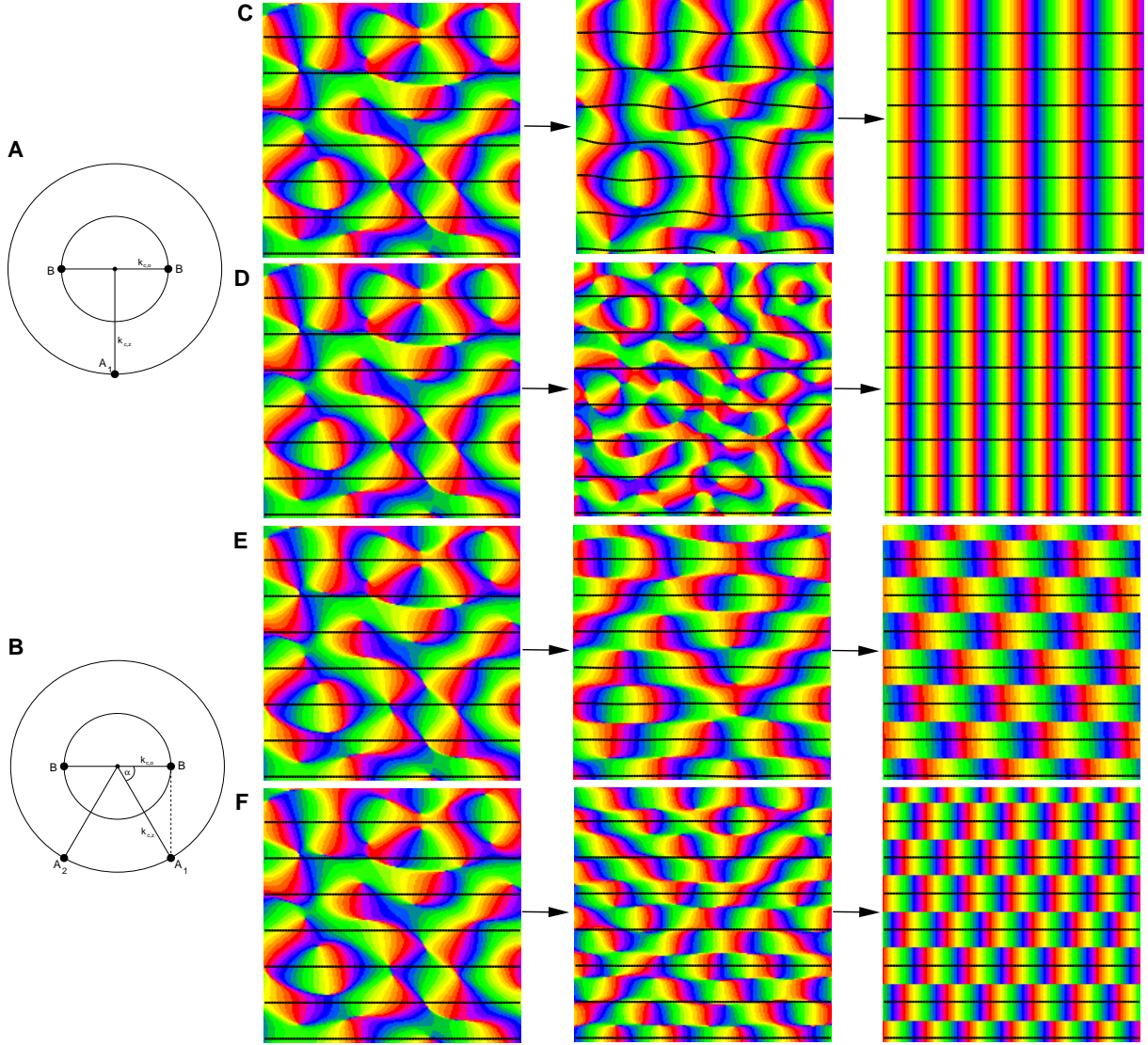


Figure 8. Map interactions with detuned wavelengths and OD stripes. OD stripes interacting with OP columns where $\Lambda_o/\Lambda_z > 1$. **A,B** Illustration of active modes in Fourier space with $k_{c,o} < k_{c,z}$, $\alpha = \arccos k_{c,o}/k_{c,z}$. **C,D** $U = \epsilon |\nabla z \cdot \nabla o|^4$, $\epsilon = 2000$, **E,F** $U = \tau o^4 |z|^4$, $\tau = 2000$, **C,E** $\Lambda_o/\Lambda_z = 1.3$, **D,F** $\Lambda_o/\Lambda_z = 2$. Left: initial condition, middle: $T = 1$, right: $T = 5 \cdot 10^4$. Parameters: $r_z = 0.05, r_o = 0.2, \Gamma_z = 20, 256 \times 256$ mesh. Initial condition identical in all simulations.

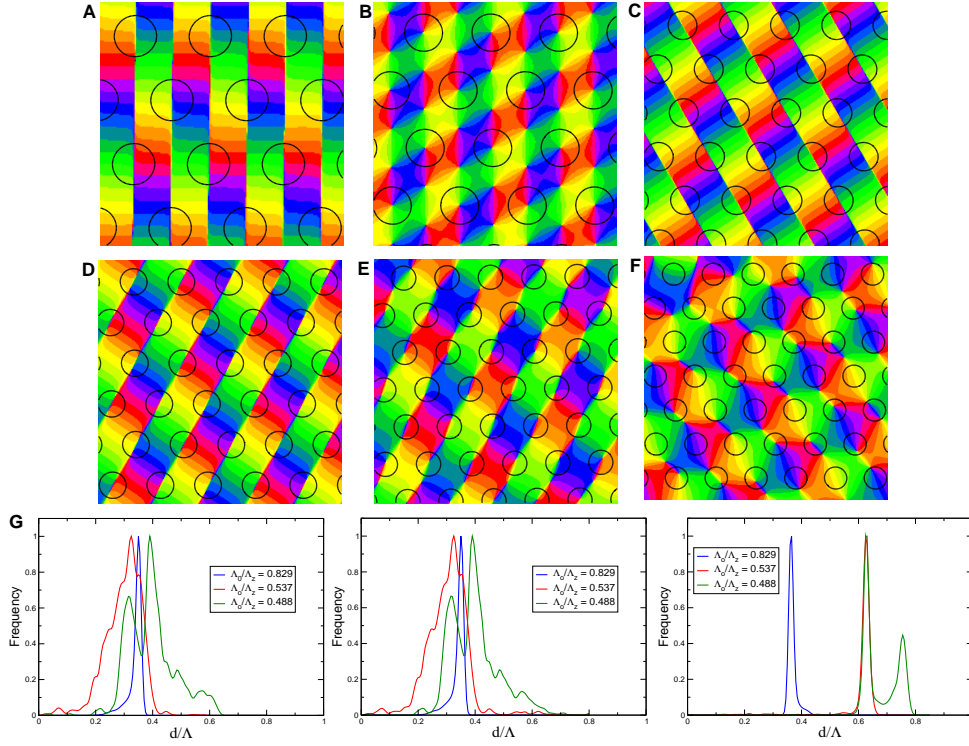


Figure 9. Map interactions with detuned wavelength and OD hexagons. $U = \epsilon |\nabla z \cdot \nabla o|^4$. **A** $\Lambda_o/\Lambda_z = 38/41 \approx 0.927$, **B** $\Lambda_o/\Lambda_z = 34/41 \approx 0.829$, **C** $\Lambda_o/\Lambda_z = 26/41 \approx 0.634$, **D** $\Lambda_o/\Lambda_z = 24/41 \approx 0.586$, **E** $\Lambda_o/\Lambda_z = 22/41 \approx 0.537$, **F** $\Lambda_o/\Lambda_z = 20/41 \approx 0.488$. **G** Distribution of nearest neighbor pinwheel distances of arbitrary (Left), opposite (Middle), and equal (Right) topological charge. Parameters: $\gamma = 0.15$, $r_z = 0.05$, $r_o = 0.2$, $\epsilon = 2000$, $\Gamma_o = 41$, $T_f = 10^4$, 256×256 mesh. Initial condition identical in all simulations.

1.6 Higher feature numbers

The inclusion of more feature dimensions into the dynamics can be performed in a similar fashion as in Eq. (9), Eq. (10) as the geometric correlations between the different types of maps seem to be qualitatively similar [9, 10, 14, 26, 40]. To illustrate this we used the higher order gradient-type inter-map coupling with three and four maps which are mutually coupled. Whereas in the case of two maps the coupling energy is zero if the two stripe solutions are perpendicular to each other the interactions between more maps can potentially lead to a frustration as not all of the individual coupling energies can simultaneously vanish. We used different, spatially irregular planform solutions as initial conditions with initial pinwheel densities $\rho \approx 3.4$ and $\rho \approx 2.4$. Using the gradient coupling energy

$$U = U_1 + U_2 + U_3 = \epsilon_1 |\nabla z \cdot \nabla o_1|^4 + \epsilon_2 |\nabla z \cdot \nabla o_2|^4 + \epsilon_3 |\nabla o_1 \cdot \nabla o_2|^4, \quad (12)$$

no OD bias ($\gamma = 0$), and equal coupling strengths $\epsilon_1 = \epsilon_2 = \epsilon_3 = \epsilon$ we observed two types of stationary solutions, see Fig. 10. In case where all bifurcation parameters were equal the OP map consisted of stripes. Also the two real fields consisted of stripes, both perpendicular to the OP stripes i.e.

$$\begin{aligned} z(\mathbf{x}) &= Ae^{i\vec{k}_1 \cdot \vec{x}} \\ o_1(\mathbf{x}) &= 2B_1 \cos(\vec{k}_2 \cdot \vec{x}) \\ o_2(\mathbf{x}) &= 2B_2 \cos(\vec{k}_2 \cdot \vec{x} + \psi), \quad \vec{k}_1 \cdot \vec{k}_2 = 0. \end{aligned} \quad (13)$$

The energy in this case is given by $U_1 = U_2 = 0$, $U_3 = \frac{B_1^4 B_2^4 \pi}{16} (18 + 16 \cos(2\psi) + \cos(4\psi))$ which is minimal for $\psi = \pi/2$, i.e. the energy is minimized by shifting one real field by one quarter of the typical wavelength. When the bifurcation parameter of the OP map was smaller than that of the two real fields we obtained PWC patterns, see Fig. 10**B**. The pinwheels were arranged such that they are in the center of a square spanned by the two orthogonal real fields and the resulting pinwheel density is $\rho = 4$. All intersection angles between iso-orientation lines and borders of the real fields were perpendicular. When extending the system by another real field we observed a similar behavior. Figure 10**C,D** shows the stationary states of a complex field coupled to three real fields. In case of equal bifurcation parameters the stationary patterns were OP stripes, perpendicular to stripe and meandering real patterns. In case the bifurcation parameter of the OP map was smaller than the other bifurcation parameters we again

observed pinwheel crystallization. Note, that in this case all pinwheels were located at the border of one of the three real fields. To summarize, pinwheel crystallization was only observed when the OP map is driven by the real field i.e. when the OP amplitudes are small. In all observed cases the patterns were spatially perfectly periodic.

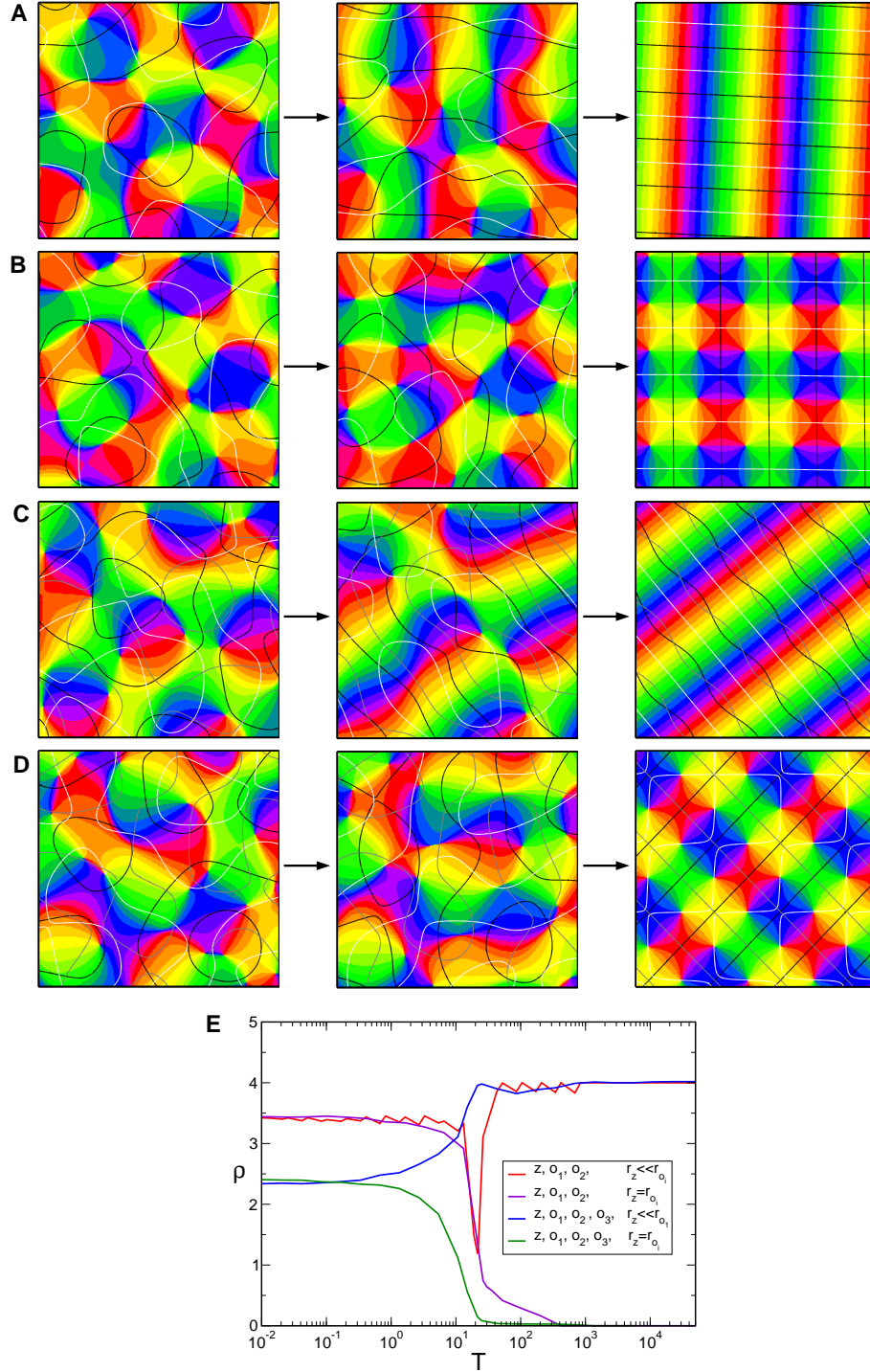


Figure 10. Map interactions in higher feature dimensions. A,B Map layout by interactions between three columnar systems ($z(\mathbf{x}), o_1(\mathbf{x}), o_2(\mathbf{x})$). All maps are mutually coupled. Superimposed on the OP map there are the borders of two real fields (black, white). **A** $r_z = r_{o_1} = r_{o_2} = 0.1$ **B** $r_z = 0.01, r_{o_1} = r_{o_2} = 0.1$. **C,D** Interactions with four columnar systems ($z(\mathbf{x}), o_1(\mathbf{x}), o_2(\mathbf{x}, t), o_3(\mathbf{x}, t)$). **C** $r_z = r_{o_1} = r_{o_2} = r_{o_3} = 0.1$. **D** $r_z = 0.01, r_{o_1} = r_{o_2} = r_{o_3} = 0.1$. Superimposed on the OP map there are the borders the of three real fields (black, gray, white). Left panel: initial conditions, middle panel: $T = 10$, right panel: $T = T_f = 5 \cdot 10^4$. **E** Time evolution of the pinwheel density. Parameters in all simulations: $\epsilon = 2000, \gamma = 0, \Gamma = 22, 128 \times 128$ mesh.

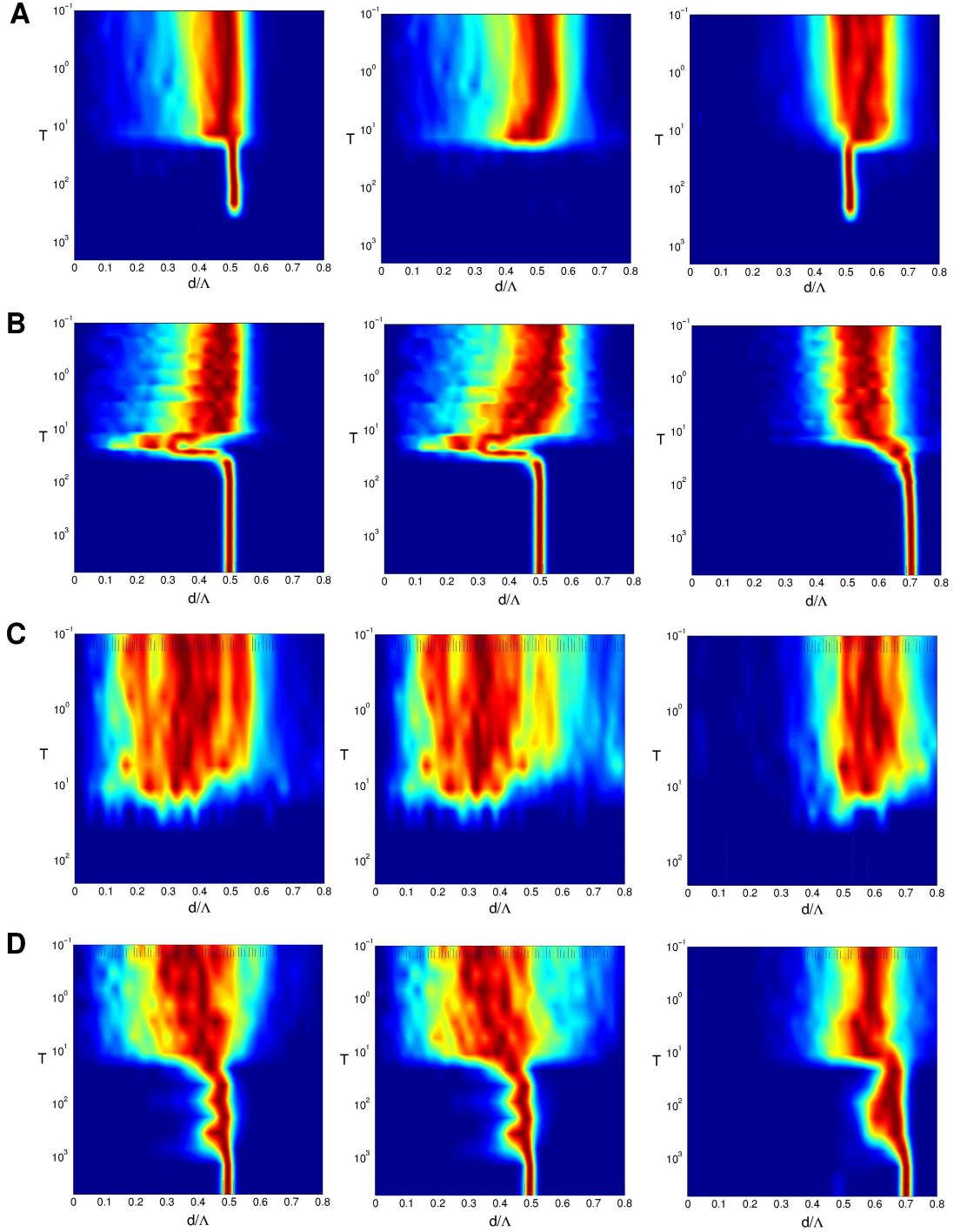


Figure 11. Distribution of nearest neighbor pinwheel distances in higher feature dimensions. Distance to the next pinwheel of arbitrary (Left), opposite (Middle), and equal (Right) topological charge. Parameters as in Fig. 10. **A,B** Map layout by interactions between three columnar systems ($z(\mathbf{x}), o_1(\mathbf{x}), o_2(\mathbf{x})$), **A** $r_z = r_{o_1} = r_{o_2} = 0.1$, **B** $r_z = 0.01, r_{o_1} = r_{o_2} = 0.1$. **C,D** Interactions with four columnar systems ($z(\mathbf{x}), o_1(\mathbf{x}), o_2(\mathbf{x}, t), o_3(\mathbf{x}, t)$), **C** $r_z = r_{o_1} = r_{o_2} = r_{o_3} = 0.1$, **D** $r_z = 0.01, r_{o_1} = r_{o_2} = r_{o_3} = 0.1$.

Discussion

Summary of results

In this and the accompanying analytical study, we presented a dynamical systems approach to the coordinated optimization of maps in the visual cortex such as OP and OD maps. In part (I) we examined in particular such analytically obtained optima of various candidate energy functionals [39]. We calculated phase diagrams for different energy functionals showing that for strong inter-map coupling pinwheel crystals are optima of the system. In the current study, we numerically analyzed the dynamics of one representative example of these coordinated optimization models. For this we focused on the high order gradient-type inter-map coupling energy that can reproduce all qualitative relationships found experimentally between OP and OD maps, does not suffer from potential OP map suppression, and has a relatively simple phase diagram near the symmetry breaking threshold. The main phenomenon characterizing the considered models, crystallization induced by coordinated optimization and inter-map coupling was verified numerically. This phenomenon was found to be robust to the influence of a weak backreaction of the OP map on the OD map, to detuning of the typical wavelengths, and was found to persist in models with higher feature space dimensionality. We characterized the complex dynamics during crystallization and calculated various pinwheel statistics. The crystalline periodic layout of pinwheel-rich solutions persisted in all studied conditions. Characterizing the behavior of transients, we found that spatially irregular transient states decayed relatively fast into locally ordered patterns during optimization.

When starting the optimization dynamics from small amplitude random initial conditions early OP patterns are essentially random orientation maps exhibiting a model insensitive, universal spatial organization throughout the initial emergence of orientation selectivity. As soon as orientation selectivity started to saturate the patterns typically reorganized towards one of a few crystalline spatial patterns. While pattern rearrangement can unfold over long timescales to achieve long-range spatial coherence, the key layout features of the crystalline target state were expressed after at most ten fold of the characteristic time of the initial growth of orientation selectivity. Similar behavior was also observed when starting near spatially irregular unstable fixed points of the orientation map dynamics.

Dynamics during the optimization process

Our study allows to examine the sequence of stages predicted for the maps under the assumption of developmental optimization. Our results consistently show that coordinated optimization models exhibit

a complex dynamics that persistently reorganizes maps over different timescales before attractors or optimized ground states are reached. Although our models exhibit various different attractor states none of the solutions converged directly to the final layout. Rather, in all of them, a substantial rearrangement of maps after initial symmetry breaking was found. As can be predicted from symmetry [22,64], at early stages of development maps must be spatially irregular if they develop from weakly tuned random initial conditions. The average pinwheel density in these early maps is bounded from below by the mathematical constant π and the distributions of nearest pinwheel distances are continuous and broad. In the models considered here, these spatially irregular early states decay over a period of the order of the intrinsic timescale after saturation of orientation selectivity. This early phase of local crystallization rapidly leads to the occurrence of different spatial domains within the pattern, with a locally stereotypical periodic layout. Even in the cases exhibiting the slowest decay of irregular patterns, this process was complete after ten intrinsic timescales. The slower dynamics that characterizes further development rearranges these domains to progressively align leading to a long-range ordered perfectly periodic crystalline array. This reorganization of patterns lasts substantially longer than the intrinsic timescale. The overall progression of states observed in our models has been found previously in numerous pattern forming dynamics both highly abstract as well as in detailed ab initio simulations [56,61,65]. PWC solutions represent attractor states and we found no other, spatially irregular, long-living states in the dynamics.

Comparing the dynamics of coordinated optimization to stages of visual cortical development

Does the observed rapid decay of irregular OP layouts into crystalline patterns speak against the biological plausibility of an optimization dynamics of the type considered here? Can one reasonably expect that a similar crystallization process could also unfold relatively rapidly during the development of the brain? Or is it more likely that what seems rapid in our numerical simulations would take very long in a biological network - potentially so long that the cortical circuitry has already lost its potential for plastic reorganization before substantial changes have occurred? To answer these questions it is important (1) to examine the fundamental timescales of the postnatal development of visual cortical circuits sub-serving orientation preference and ocular dominance, (2) to discuss how these timescales can be compared to the formal timescales that appear in dynamical models of map formation and reorganization and (3) to examine whether there is any biological evidence for a secondary rearrangement of orientation and ocular dominance maps subsequent to their initial establishment.

Because all reorganization processes predicted by our models occur after the saturation of single cell selectivities these questions are in fact essential to assess the explanatory power of the model. The predicted reorganization processes can only be reasonably compared to the course of biological development, if there is a period of ongoing cortical circuit plasticity that is substantially longer than the time needed to reach mature levels of single cell selectivity. The applicability of any dynamical model beyond the emergence of single cell selectivity would be fundamentally questioned if an arrested-development scenario would be adequate. Such an arrested-development scenario would imply that some random pattern emerging initially is effectively frozen by the termination of the period of developmental plasticity. In this case, viewing cortical development as an optimization process were to offer only very limited insight: Because the early emerging states are model insensitive [22, 64, 66, 67] the same kind of frozen states would be predicted by interrupted optimization of very different energy functionals. This would have two distinct consequences: (1) biological observations on map structure would not contain much information to separate adequate from inadequate models of map formation and optimization and (2) none of these energy functionals could serve as a compact and specific description of the design principles ruling cortical functional architecture.

Let us first discuss the duration of the process of establishing mature saturated levels of stimulus selectivity from weakly selective initial conditions from a theoretical perspective. All models for the development of visual cortical functional selectivity from an unselective or weakly selective initial condition are known to exhibit a distinct intrinsic time scale for the emergence of stimulus selectivity in individual neurons [36, 47, 49, 68–70]. In the abstract order parameter models examined here this time scale is set by the inverse of the maximum eigenvalue r_z . It is important to note that this time scale represents an effective parameter describing a collective circuit property and that this parameter is not rigidly related to any particular cellular or synaptic timescale such as e.g. the characteristic time required for the expression of LTP, spine growth, homeostatic plasticity or other functional or morphological synaptic changes. Theoretical studies of microscopic models in which the effective time scale was explicitly calculated have established that this time scale depends (1) on the ensemble of activity patterns driving development and also (2) on characteristics of the local cortical circuits [54, 70, 71]. For instance in a representative, analytically solvable microscopic model for the emergence of ocular dominance patterns the maximum

eigenvalue is given by

$$\lambda_{max} = -\frac{\sigma^2}{\tau_{syn}} + \frac{1}{\tau_{syn}} \int d^2x (C_L(x) + C_R(x) - 2C_{LR}(x))$$

where τ_{syn} is the characteristic time scale for synaptic changes, σ measures the spatial extend of co-activated neuron groups in the model cortex and C_L , C_R and C_{LR} are auto- and cross-correlation functions of the activity patterns in the left and right eye layers of the LGN [54]. While the effective time scale for the emergence and saturation of selectivity is expected not to be faster than the fundamental processes of synaptic change, they can certainly be substantially slower.

The best way to obtain an estimate for the intrinsic time scale of map dynamics in the developing visual cortex is thus to consider the empirically observed duration of the respective processes under normal conditions. For orientation selectivity in the primary visual cortex this information has been obtained conclusively for cat and ferret. In both species orientation selectivity is established starting from an initial condition in which cells are only weakly orientation biased and it takes a period between a few days and at most one week to reach mature levels of single cell orientation selectivity [11, 17, 21, 72–74]. It is noteworthy that similar time scales are also sufficient for substantial morphological changes of thalamo-cortical axonal structure [75]. Even in anesthetized animals, visual cortical preferences for stimulus orientation or direction, or preference for one eye all can undergo substantial activity induced changes within a few hours [76–80]. The characteristic time scale for the emergence and maturation of single cell stimulus selectivities can thus be constrained with good confidence to be of the order of at least a few hours and at most one week.

The second time scale that needs to be estimated empirically is the duration of the period over which juvenile levels of developmental plasticity in visual cortical circuits are maintained. This period can be narrowed down by considering the period of susceptibility for modification of cortical neuronal preferences by changes of visual experience. For this, it is to be kept in mind that statements on the duration of such periods of susceptibility invariably depend on a particular type of modification of visual experience and specific circuit involved [21, 73, 81]. The temporal extend of a period of plasticity has been addressed most comprehensively for the modification of ocular dominance by monocular deprivation in the cat visual cortex. Ocular dominance plasticity is mediated by thalamo-cortical projections. Thalamo-recipient neurons in the cat visual cortex are also the first neurons in the thalamo-cortical visual pathway which

exhibit orientation selectivity and thalamo-cortical connections are thought to define the preferred orientation of cortical columns in the cat (see e.g. [82]). It is thus plausible to assume that ocular dominance plasticity is probing the plasticity of circuitry underlying both orientation preference and eye dominance. It is conceivable in principle that the features of thalamo-cortical circuitry that define the preferred orientation - although mediated by the same synapses - are much less susceptible to modification than those defining eye dominance. The emergence of distinct receptive field features appear to be differentially sensitive to the ablation of particular synaptic molecular components, indicating that the emergence of orientation selectivity requires a temporally more precise synaptic transmission than ocular dominance segregation and plasticity [83]. An explicit mechanism, however, that could terminate plasticity of orientation preference while preserving it for ocular dominance, has neither been identified experimentally nor theoretically. On the contrary, Fregnac and coworkers in classical microstimulation studies found that the very same stimulation strategy that was effective in changing the ocular dominance of visual cortical neurons during the ocular dominance critical period was also effective in inducing changes of their preferred orientations [76–78]. In addition, reversal of monocular deprivation in area 17 (but not area 18) can induce the formation of different preferred orientations in the left and right eye receptive fields of a neuron [84–86]. Overall the available evidence in the cat thus supports the view that ocular dominance plasticity probes the plasticity of neuronal circuitry critical to both ocular dominance and orientation preference. We will summarize the current evidence that the orientation preference of cortical neurons in fact changes during the critical period for monocular deprivation in the section 'Juvenile plasticity can support an ongoing reorganization of orientation preference and ocular dominance' below.

How long does the period of juvenile ocular dominance plasticity last? In the field of visual cortical development, there is a broad and well established consensus that the period of susceptibility to monocular deprivation in the cat lasts for several months of postnatal life [73, 84, 87–89]. The primary visual cortex of the cat is maximally susceptible to monocular deprivation in kitten of four weeks of age [84, 87, 88]. The initial establishment of orientation preference and ocular dominance maps in kittens occurs around the time of eye opening in the second postnatal week [72, 74]. Maximal sensitivity is thus reached two weeks after the emergence of maps and the onset of normal vision. After the first postnatal month susceptibility to monocular deprivation was found to gradually decline back to levels comparable to those present at the onset of vision and initial map emergence. The closure of the period of developmental plasticity was estimated by several studies to occur between the 14th and 18th postnatal week [84, 87, 88]. This is 12 to

16 weeks after single neurons first exhibit adult like levels of orientation selectivity and eye dominance. Later studies, found that substantial modifications of responses could be induced even up to the 35rd postnatal week [89].

The available data thus indicate a clear separation of timescales between the duration of the period of developmental plasticity and the characteristic time scale for the emergence of stimulus selectivity and maps. The duration of the relevant period of developmental plasticity is at least 10 times longer (e.g. 12 weeks vs. 1 week) and potentially more than three orders of magnitude longer (32 weeks vs. 6 hours) than the characteristic time scale for the emergence of stimulus selectivity and maps. This estimate rests on the idealizing assumption that the characteristic time scale of map dynamics remains essentially constant over the duration of the critical period. An assumption that is not easy to check and not likely to be exactly fulfilled. If the time constant was to rapidly increase after the initial generation of the maps, the separation of time scales would be less pronounced. However, the susceptibility to ocular dominance plasticity, in fact, increases after eye opening and initial map formation and returns to levels as low as during initial map establishment only at the end of the critical period [84, 88]. A higher degree of plasticity during the period of juvenile plasticity would be rather consistent with a more speedy process i.e. a reduced time constant than with an increased, i.e. slowed, down time constant. This observation thus suggests that our estimate rather under estimates than over estimates the separation of the two time scales.

We emphasize that we are certainly not the first to point out this substantial separation of time scales. To our best knowledge, Jack Pettigrew was the first to highlight and discuss the issues and question raised by this fact of cortical circuit development in his essay entitled *The paradox of the critical period for striate cortex* ([90], see discussion in [91]). Specifically with respect to modeling the dynamics of functional cortical architecture during early development this aspect has been considered previously particularly in [22, 42, 66, 92].

When does a dynamical model successfully explain adult functional cortical architecture?

In light of the above considerations it appears of limited value to compare maps from a simulation obtained when selectivity first reaches mature levels to biological patterns present in the adult cortex. Maps in the adult visual cortex of the cat have been subject to more than ten weeks of ongoing plasticity. They are therefore better viewed as dynamic equilibria that are largely maintained under a continuous process of ongoing activity-driven synaptic turnover. Current experimental evidence, nevertheless, indicate that

the maps emerging initially over the first days of normal vision exhibit many layout properties that are preserved throughout the juvenile period of plasticity and into adulthood [11, 42]. Taking the long duration of the period of juvenile plasticity into account, this is likely to mean that these properties have been actively maintained by an ongoing dynamics.

Our current results as well as many prior theoretical studies (reviewed in [42], supplement) clearly demonstrate that the requirement to generate and maintain a realistic column layout is a much more selective criterion for the identification of appropriate candidate models than the mere ability to initially generate good looking maps. It is thus a more stringent test of a dynamical models explanatory power to compare the maps obtained at later stages to the biologically observed functional organization of the visual cortex. Our estimates suggest that it would be reasonable to require of a biologically plausible model that states which resemble the adult functional architecture occur in time between one and three orders of magnitude later than the maturation of average selectivity. Using this criterion, the states observed in our simulations in fact suggest that the considered models are not capable of explaining the biological organization in a satisfying fashion: Patterns observed between 10 and 1000 intrinsic timescales are dominated by crystalline local arrangements that are distinctly different from the spatially irregular layout of orientation maps observed in both juvenile and adult visual cortex.

Juvenile plasticity can support an ongoing reorganization of orientation preference and ocular dominance

The comparison of patterns at between 10 and 1000 intrinsic timescales suggests that the maintained plasticity that is ongoing at least until the end of the critical period has features not present in the models examined here. Biologically, this conclusion would be completely compulsory, if there was direct evidence that the period of juvenile plasticity in fact included a substantial reorganization of visual cortical functional organization after the initial emergence of single cell selectivity. This would constitute direct evidence that the initially emerging set of stimulus preference is in fact not frozen and that the duration of the period of juvenile plasticity is of sufficient duration to allow a secondary reorganization of the maps.

Recently, evidence that ongoing plasticity enables ongoing pattern reorganization has started to accumulate both for species exhibiting a columnar functional architecture as well as for the rodent typical non-columnar salt-and-pepper organization of stimulus preferences [91, 93, 94]. For cat visual cortex, Kaschube and coworkers have demonstrated that the spatial organization of orientation columns in stri-

ate cortex is progressively reorganized between the sixth and the 14th postnatal week such that the organization of orientation columns that are reciprocally connected to extra-striate visual cortex and contra-lateral hemisphere striate cortex are better matched [91]. A second line of evidence is related to the fact that the surface area of cat striate cortex substantially increases postnatally [93,95–97]. The spatial periodicity of both orientation as well as ocular dominance columns, however, remains basically unaffected during this period [91,93,98]. Keil and coworkers have reported evidence that this areal growth in the presence of maintained mean column spacing induces a characteristic spatial reorganization of the layout of ocular dominance columns within cat striate cortex [93]. Growth related rearrangement of orientation columns had been suggested previously from observations on a smaller data set from juvenile macaques [63].

Perhaps the most striking demonstration that the functional preferences of visual cortical neurons can reorganize over long time scales during the period of juvenile plasticity has emerged from studies of the mouse visual cortex. In the mouse, as in cat, visual cortical neurons first develop orientation selectivity around the time of first eye opening in the second postnatal week [94,99]. Mimicking the developmental time course in the cat, also the duration of the period of juvenile plasticity in the mouse is quite long and extends beyond the third postnatal month [100,101]. At a duration of more than 10 weeks, it is thus substantially longer than required for the expression of adult-like single neuron selectivities. Wang and coworkers recently demonstrated that neurons in the binocular segment of mouse visual cortex in fact change their preferred orientations during this period [99]. Neurons in the binocular segment of mouse striate cortex were found to first exhibit widely different preferred orientations in the left and right eye. The two different preferred orientations then underwent secondary reorganization and became matching at an age of 5 weeks postnatally [99]. Such late changes might not be restricted to the binocular segment of the mouse visual cortex. In the monocular segment, Rochford and coworkers documented substantial changes in the complement of preferred orientations and preferred directions represented between eye opening and the first postnatal month [94]. An adult-like composition of orientation selectivities was not found before the end of the second postnatal month [94]. It might be interesting to note that a substantial long-term reorganization of cortical preferences has also been recently demonstrated in the rat barrel cortex [102]. Kremer and coworkers found that preferences for the direction of whisker deflection reorganize over the course of the first three postnatal months. Long-term reorganization might thus potentially constitute a general feature of sensory cortical representations.

Experimental evidence thus clearly supports that the circuits underlying ocular dominance and orientation selectivity remain in a state of flux for weeks and months after the initial emergence of visual responsiveness and stimulus selectivity. We conclude that the model considered in the present study is - in its present form incapable of reproducing the maintenance of visual cortical architecture of primates and carnivores in a convincing manner. This conclusion presumably also applies to all models examined in the accompanying analytical study. In none of them did we find a stable state or minimum energy pattern that would reproduce the layout of orientation columns in the visual cortex. It is thus predicted for all of them that spatially irregular states, if formed transiently, will decay into biologically unrealistic crystalline patterns. How such models could be modified to better reproduce the observed spatially irregular layout of cortical columns will be discussed subsequently in the section 'Generality of pinwheel crystallization'.

Conditions for pinwheel stabilization

The analytical results presented in part (I) showed that in several models OD stripes are not able to stabilize pinwheels near symmetry breaking threshold and for only one real-valued scalar field. This result appeared to be insensitive of the specific type of inter-map interaction [39]. Our numerical results show that this result is also insensitive to a detuning of typical wavelengths. For different ratios of the typical wavelengths of OP and OD pinwheel-rich patterns either decay into pinwheel-free OP stripes or patterns with OP fracture lines when interacting with OD stripes. These findings support the conclusion that in models for the joint optimization of OP and OD maps a patchy OD layout is important for pinwheel stabilization by crystallization. One should note, however, that sufficiently far above threshold dislocations in the OD map can become frozen [103]. Via inter-map coupling these dislocations could prevent pinwheels to completely annihilate and thus lead to local pinwheel stabilization near OD dislocations.

In the current study we also generalized our dynamical systems approach to include any additional number of columnar systems. One reason to consider additional visual cortical maps originates from the finding that the removal of the OD map in experiments does not completely destabilize pinwheels [29]. Moreover, in tree shrews, animals which completely lack OD columns, OP maps contain pinwheels and exhibit a pinwheel arrangement essentially indistinguishable from species with columnar OD segregation [13]. This might reflect the influence of additional columnar systems like spatial frequency columns that can be expected to interact with the OP map in a similar fashion as OD columns [40]. From a theoretical perspective, one might suspect that couplings between more than two systems that promote

a mutually orthogonal arrangement are harder to satisfy the more maps are considered. In principle this could lead to the emergence of irregular patterns by frustration. In numerical simulations we examined coordinated optimization with three and four columnar systems. In these cases pinwheel stabilization is possible even without an OD bias. The resulting stationary OP patterns are, however, still either stripes or PWC solutions. For more than two feature maps, asymmetry of one feature dimension is thus not a necessary condition for pinwheel stabilization by coordinated optimization.

We also characterized the dynamics of pinwheel crystallization from pinwheel-free initial conditions. With the analytical approach presented in part (I) we were able to show that pinwheel-rich solutions correspond to the energetic ground state of our models for large inter-map coupling [39]. This can be reflected by simulations in which pinwheels are created even when starting from an initial OP stripe pattern. Assessing pinwheel creation from pinwheel-free initial conditions could more generally serve as a simple test for the existence of a pinwheel-rich attractor state in models of OP development that can be applied to models of arbitrary complexity. One should note, however, that the production of pinwheels from a pinwheel-free initial condition provides only a sufficient but not necessary criterion to verify the existence of a pinwheel-rich attractor state. This criterion may be violated if pinwheel-free and pinwheel-rich attractor states coexist. Nevertheless, the pinwheel production criterion can be used to demonstrate that pinwheels are not just a remnant of random initial conditions.

Generality of pinwheel crystallization

Pinwheel crystals have been previously found in several abstract [66, 104] as well as in detailed synaptic plasticity based models [68, 105, 106]. Remarkably, in a model of receptive field development based on a detailed dynamics of synaptic connections the resulting OP map showed a striking similarity to the hPWC presented above, compare Fig. (6) and [39, 105]. These observations indicate that pinwheel crystallization is not an artefact of the highly idealized mathematical approach used here. In fact, the first OP map predicted ever by a synaptically based self-organization model presented by von der Malsburg in 1973 exhibited a clearly hexagonal column arrangement [68]. Von der Malsburgs calculations as well as those presented in [105] utilized a hexagonal grid of cells that may specifically support the formation of hexagonal patterns. Our numerical and analytical results clearly demonstrate that patterns of hexagonal symmetry do not critically depend on the use of a hexagonal grid of cells. As our simulations can generate hexagonal pattern also for square lattices of cells it would be instructive to revisit von der Malsburgs model implemented for other grids both of square symmetry as well as for irregular positions of cells. In

our study, we examined whether the non-crystalline layout of visual cortical maps could result from a detuning of OP and OD wavelengths. However, while destabilizing hPWC solutions, wavelength detuning leads to spatially perfectly regular solutions in all studied cases. This suggests that a spatially regular layout is not an exceptional behavior in models of the coordinated optimization of visual cortical maps that would require fine tuning of parameters.

The reason for the strong differences to experimentally observed maps might thus be the presence of biological factors neglected in the models examined here. Such factors might be a greater distance from the pattern formation threshold, different kinds of biological noise, or the presence of long-range neuronal interactions. Vinals and coworkers demonstrated for the case of stripe patterns that a Swift-Hohenberg model far from the bifurcation point can exhibit stable disclination defects [103]. Although the results indicate only a spatially sparse set of stabilized defects it will be interesting to examine whether this also applies to the case of multidimensional coupled Swift-Hohenberg models and to establish which properties model solutions develop very far from the bifurcation point. Theoretically, it is well understood that in principle so called 'nonadiabatic effects' can induce the pinning of grain boundaries in pattern forming media [107–110]. In one spatial dimension and for models with several interacting order parameter fields similar mechanisms may even lead to the emergence of spatially chaotic solutions [111–113]. These studies suggest to examine whether spatial incommensurability far from threshold can induce spatially chaotic patterns in one and two dimensional coordinated optimization models. Such studies may uncover a completely novel scenario for explaining the emergence of spatially irregular states in models of cortical map optimization.

A second interesting direction will be the inclusion of frozen spatial disorder in models for the self-organization of multiple cortical maps. Such disorder could represent a temporally fixed selectivity bias that favors particular feature combinations at different position in the cortical sheet. For orientation preference, the proposals of Waessle and Soodak recently revisited by Ringach and coworkers that retinal ganglion mosaics might constrain and seed orientation column patterns would represent a specific mechanisms for such a fixed local bias [114–118]. Experimental evidence that retinal organization can impose local biases was revealed by Adams and Hortons finding that the pattern of retinal blood vessels can specifically determine the layout of ocular dominance columns in squirrel monkey visual cortex ([119, 120], for a modelling study see also [121]). Spatial disorder terms in an equation can also be designed to model randomness in the interactions between neurons at different positions. This might

result from heterogeneities in lateral interactions within the cortical sheet. In particular this later type of modification has been examined in simple examples of order parameter equations and was found to qualitatively change the type of the bifurcation and the nature of the unstable modes [122–125]. It will be important to investigate how different types of spatial disorder modify the behavior of models derived from biologically meaningful energy functionals. We hope that for such studies of the influence of ‘biological noise’ a thorough understanding of the properties of perfectly homogeneous and isotropic systems as achieved here will provide a solid basis for disentangling the specific contributions of randomness and self-organization.

Finally, a third promising direction for modifying the type of models considered here is the inclusion of long-ranging intra-cortical interaction in the equations for the individual order parameter fields. The impact of long-ranging intra-cortical interactions has been studied previously both with respect to the properties of patterns emerging during the phase of initial symmetry breaking [32, 126–128] as well as for its influence on long-term pinwheel stabilization and pattern selection [67, 92, 129]. Models for orientation maps that include orientation-selective long-ranging interactions exhibit a good quantitative agreement of both attractors and transient states to the biological organization of orientation preference maps in the visual cortex [42]. Including orientation-selective long-ranging interactions in models for the coordinated optimization of multiple cortical maps could provide a transparent route towards constructing improved models for the coordinated optimization of column layouts matching the spatial structure of orientation maps.

Experimental evidence for hexagonal orientation column patterns

Recently, Paik and Ringach have argued that a roughly hexagonal arrangement of iso-orientation domains would provide evidence for a defining role of retinal ganglion cell mosaics for the spatial arrangement of orientation columns [114, 117, 118]. It is interesting to consider this claim in view of our results as well as in view of the wealth of activity-dependent models that predict hexagonal arrangements irrespective of the arrangement of retinal ganglion cells [67, 92, 105, 130–132]. Since all of these distinct models are known to generate hexagonal arrays of orientation columns it seems questionable to view evidence for a hexagonal arrangement as evidence for a particular activity-independent mechanism. Our characterization of the dynamics of crystallization, however, enables to identify more selective predictions of a retinal ganglion cell mosaic based formation of hexagonal iso-orientation domains. If the pattern of OP columns is seeded by retinal ganglion cell mosaics, as initially proposed by Soodak [115] and recently re-articulated by Paik

and Ringach [114], hexagonal structures should be detectable from the very beginning of development, i.e. already at stages when orientation selectivity is still increasing. Hexagonal PWCs in self-organizing models, in contrast, form from an initially irregular and isotropic state. Thus the time dependence of hexagonal-like column arrangements can distinguish in principle between self-organized as opposed to retinal ganglion cell mosaic imprinted hexagonal arrangements. As we found in all models examined hexagonal arrangements are frequently of rather high pinwheel density of about 5 pinwheels per hyper-column. Also the hexagonal pattern constructed by Paik and Ringach appear to exhibit relatively high pinwheel density of $\rho \approx 3.5$. Thus both theories appear inconsistent with observed pinwheel densities. A mixed scenario in which retinal ganglion cell mosaics seed the initial pattern of iso-orientation domains and later activity-dependent refinement drives a rearrangement of OP maps towards the experimentally observed design therefore predicts a substantial degree of net pinwheel annihilation. Kaschube et al. presented evidence for essentially age independent pinwheel densities in ferret visual cortex starting between 5 to 20 postnatal weeks. No indication of substantial pinwheel annihilation is visible in this data [42]. One should note that in ferret visual cortex orientation columns first arise in the fifth postnatal week [11]. The relation of the analysis by Paik and Ringach and the statistical laws described by Kaschube and coworkers ask for further analysis and comparison.

A hierarchy of visual cortical maps

In the current studies we focused on a particular hierarchy of visual cortical maps. In the analytical calculations and most simulations the OD map was assumed to be dominant which corresponds to a choice of control parameters that satisfy $r_o \gg r_z$. That maps form a hierarchy under such conditions can be seen from the limiting case in which inter-map interactions become effectively unidirectional. In this case the dynamics of the OP map is influenced by OD segregation while the OD dynamics is effectively autonomous. This limit substantially simplifies the analysis of map-interactions and the identification of ground states. The effect of a backreaction on the OD map can be studied within the presented approach either by solving amplitude equations numerically or by solving the full field dynamics. We observed that, although the presented optima persist, with increasing backreaction on the OD map the minimum inter-map coupling strength necessary for the stability of hexagonal pinwheel crystals increases. By solving the full field dynamics numerically we confirmed this conclusion. In the presented numerical simulations the backreaction, however, was relatively small. The simulations nevertheless establish that our results are not restricted to the limit $r_z/r_o \rightarrow 0$ i.e. that this regime does not represent a singular limit. A

comprehensive analysis of the effect of strong backreaction is beyond the scope of the current study. One should note that the decoupling limit $r_z/r_o \rightarrow 0$ does not lead to completely unrealistic OD patterns. In particular, compared to the architecture of macaque visual cortex the uncoupled OD dynamics has stationary patterns which qualitatively well resemble the layout of observed OD maps. Macaque primary visual cortex appears to exhibit essentially three different kinds of OD patterns: Fairly regular arrays of OD stripes in most of the binocular part of the visual field representation, a pattern of ipsilateral eye patches in a contralateral background near the transition zone to the monocular segment and of course a monocular representation in the far periphery. These might correspond to the three fundamental solutions of the OD equation: stripes, hexagons, and a constant solution, which are stable depending on the OD bias (see Figure (16) of [39]). In cat visual cortex the observed OD layout is patchy [46, 133–136].

Modeling areal borders and experimentally induced heterogeneities

Viewed from a formal perspective, the presented theoretical approach offers also convenient ways to model the impact of spatial inhomogeneities in the visual cortex on OP map structure. For this purpose, the co-evolving field does not represent a feature map but would be designed to describe a real or artificial areal border or a disruption of local circuitry. To this end, the OP map would be coupled, using low order coupling energies, to a fixed field describing the areal border such that its values are for instance one inside and minus one outside of the area with a steep gradient interpolating between the two. Outside the areal border a strong coupling to such a field can lead to complete suppression of orientation selectivity. Using a gradient-type inter-map coupling energy inter-map coupling can also be used to favor a perpendicular intersection of iso-orientation lines with the areal borders as observed in some experiments [13, 137]. Artificial heterogeneities and areal borders have been induced by local ablation or other local surgical interventions [137]. Viral approaches such as the silencing of cortical regions by transfection with hyperpolarizing ion-channels now make it possible to impose them with minimal intervention and potentially in a reversible fashion [138, 139].

Conclusions

The presented models for the coordinated optimization of maps in the visual cortex, that were studied analytically in part (I) and numerically in part (II), lead in all studied conditions to spatially perfectly regular energy minima. In local regions on the order of a few hypercolumn areas, column layout rapidly converges to one of a few types of regular repetitive layouts. Because of this behavior the considered models cannot robustly explain the experimentally observed spatially irregular common design of OP maps in

the visual cortex. As expected from these qualitative differences all pinwheel statistics considered, exhibit strong quantitative deviations from the experimentally observed values. These findings appear robust with respect to finite backreaction, detuning of characteristic wavelengths, and the addition of further feature space dimensions. Recent work demonstrated that the spatially irregular pinwheel-rich layout of pinwheels and orientation columns in the visual cortex can be reproduced quantitatively by models that represent only the orientation map but include long-range interactions [42,67,92]. In the visual cortex of species widely separated in mammalian evolution we previously found virtually indistinguishable layout rules of orientation columns that are quantitatively fulfilled with a precision of a few percent [42]. In view of these findings the current results suggest that models in which pinwheel stabilization is achieved solely by coordinated optimization and strong inter-map coupling are not promising candidates for explaining visual cortical architecture. In order to achieve a quantitatively more viable coordinated optimization theory one might consider taking additional 'random' factors into account. One should however not conclude that coordinated optimization does not shape visual cortical architecture. Using the general approach developed here it is possible to construct a complementary type of models in which the complex OP map is dominant. Such models, using non-local terms in the energy functional of the OP map, can be constructed to reduce to the model in [42,67,92] in the weak coupling limit. Because long-range interaction dominated models can reproduce the spatially irregular layout of OP maps, one expects from such models a better reproduction of the observed architecture for weak coupling. Alternative scenarios might emerge from the inclusion of quenched disorder or very far from the pattern formation threshold. Because of its mathematical transparency and tractability the approach developed in the present studies will provide powerful tools for examining to which extent such models are robust against coupling to other cortical maps and to disentangle the specific contribution of coordinated optimization to visual cortical architecture.

Methods

Tracking and counting pinwheels

During the evolution of OD and OP maps we monitored the states from the initial time $T = 0$ to the final time $T = T_f$ using about 150 time frames. To account for the various temporal scales the dynamics encounters the time frames were separated by exponentially increasing time intervals. Pinwheel centers

were identified as the crossing of the zero contour lines of the real and imaginary parts of $z(\mathbf{x})$. During time evolution we tracked all the pinwheel positions and, as the pinwheels carry a topological charge, we divided the pinwheels according to their charge. The distribution of pinwheel distances indicates the regularity and periodicity of the maps. Therefore we calculated the minimal distance between pinwheels, measured in units of the column spacing Λ during time evolution. In simulations we used periodic boundary conditions. In order to correctly treat pinwheels close to map borders we periodically continued the maps. Nearest neighbors of pinwheels are thus searched also in the corresponding periodically continued maps.

The rearrangement of OP maps leads to annihilation and creation of pinwheels in pairs. Between two time frames at T_i and T_{i+1} we identified corresponding pinwheels if their positions differed by less than $\Delta x = 0.2\Lambda$ and carry the same topological charge. If no corresponding pinwheel was found within Δx it was considered as annihilated. If a pinwheel at T_{i+1} could not be assigned to one at T_i it was considered as created. We define the pinwheel creation $c(t)$ and annihilation $a(t)$ rates per hypercolumn as

$$c(t) = \frac{dN_c}{\Lambda^2 dt}, \quad a(t) = \frac{dN_a}{\Lambda^2 dt}, \quad (14)$$

where N_c and N_a are the numbers of created and annihilated pinwheels. Creation and annihilation rates were confirmed by doubling the number of time frames.

To what extent are the pinwheels of the final pattern just rearrangements of pinwheels at some given time T ? To answer this question for a given set of pinwheels at an initial time $T = T^*$ we further calculated the fraction $s(t)$ of those pinwheels surviving until time T . Finally, the fraction of pinwheels present at time T^* that survive up to the final time $T = T_f$ is given by $p(t)$.

Numerical integration scheme

As the Swift-Hohenberg equation is a stiff partial differential equation we used a fully implicit integrator [140]. Such an integration scheme avoids numerical instabilities and enables the use of increasing step sizes when approaching an attractor state. The equation

$$\partial_t z(\mathbf{x}, t) = \hat{L}z(\mathbf{x}, t) - N[z(\mathbf{x}, t)], \quad \hat{L} = r - (k_c^2 + \Delta)^2, \quad (15)$$

is discretized in time. Using a Crank-Nicolson scheme this differential equation is approximated by the nonlinear difference equation

$$\frac{z_{t+1} - z_t}{\Delta t} = \frac{\left(\hat{L}z_{t+1} + N[z_{t+1}]\right) + \left(\hat{L}z_t + N[z_t]\right)}{2}. \quad (16)$$

This equation is solved iteratively for z_{t+1} with the help of the Newton method which finds the root of the function

$$G[z_{t+1}] = \left(-\hat{L} + \frac{2}{\Delta t}\right) z_{t+1} - N[z_{t+1}] - \left(\left(\hat{L} + \frac{2}{\Delta t}\right) z_t + N[z_t]\right). \quad (17)$$

The field $z(\mathbf{x})$ is discretized. For a grid with N meshpoints in the x -direction and M meshpoints in the y -direction this leads to an $M \times N$ dimensional state vector \mathbf{u} . Discretization is performed in Fourier space. The Newton iteration at step k is then given by

$$DG(\mathbf{u}^k)\Delta\mathbf{u}^k = -G(\mathbf{u}^k), \quad \mathbf{u}^{k+1} = \mathbf{u}^k + \Delta\mathbf{u}^k, \quad (18)$$

with DG the Jacobian of G . Instead of calculating the matrix DG explicitly a matrix free method is used, where the action of the matrix is approximated using finite differences. To solve the linear system $A\mathbf{x} = \mathbf{b}$ with $A = DG(\mathbf{u}^k)$, $\mathbf{b} = -G(\mathbf{u}^k)$ we used the Krylov subspace method [140]. The Krylov subspace of dimensionality k is defined as

$$\mathcal{K}_k(A, \mathbf{v}_1) = \text{span}\{\mathbf{v}_1, A\mathbf{v}_1, A^2\mathbf{v}_1, \dots, A^{k-1}\mathbf{v}_1\}. \quad (19)$$

In the *Generalized Minimum Residual* (GMRES) algorithm the Krylov subspace is generated by $\mathbf{v}_1 = \mathbf{r}_0/|\mathbf{r}_0|$ with $\mathbf{r}_0 = A\mathbf{x}_0 - \mathbf{b}$, and \mathbf{x}_0 an initial guess, see [140]. After k iterations, the refined solution is given by

$$\mathbf{x}_k = \mathbf{x}_0 + V_k\mathbf{y}, \quad (20)$$

where the matrix $V_k = (\mathbf{v}_1, \dots, \mathbf{v}_k)$ has the base vectors of the Krylov subspace as its columns. The vector \mathbf{y} is chosen by minimizing the residuum

$$\|\mathbf{b} - A\mathbf{x}_k\|_2 = \|\mathbf{r}_0 - AV_k\mathbf{y}\|_2 \stackrel{!}{=} \min, \quad (21)$$

where $\|\cdot\|_2$ denotes the Euclidean norm. For this procedure an orthonormal basis of the Krylov subspace is generated with an Arnoldi process. With the use of the similarity transformation

$$AV_k = V_{k+1}\tilde{H}_k, \quad (22)$$

where \tilde{H}_k is an upper Hessenberg matrix, $\mathbf{v}_1 = \mathbf{r}_0/|\mathbf{r}_0|$, and the orthogonality of V_k , the optimality condition Eq. (21) becomes

$$\|\tilde{H}_k\mathbf{y} - |\mathbf{b}|\mathbf{e}_1\|_2 \stackrel{!}{=} \min, \quad (23)$$

with $\mathbf{e}_1 = (1, 0, \dots, 0)$ the first unit vector of dimension $k + 1$. For a \mathbf{y} that minimizes this norm the approximate solution is given by $\mathbf{x}_k = \mathbf{x}_0 + V_k\mathbf{y}$. To improve the convergence of this iterative method preconditioning was used. A preconditioner M is multiplied to $A\mathbf{x} = \mathbf{b}$ such that $M^{-1}A$ is close to unity. A preconditioner suitable for our model is the inverse of the linear operator in Fourier space with a small shift $0 < \epsilon \ll 1$ in order to avoid singularities i.e.

$$M = \left(\epsilon + (k^2 - k_c^2)^2 + \frac{2}{\Delta t} \right)^{-1}. \quad (24)$$

The convergence of Newton's method is only guaranteed from a starting point close enough to a solution. In the integration scheme we use a line search method to ensure also a global convergence [141]. Newton's method Eq. (18) is thus modified as

$$\mathbf{u}^{k+1} = \mathbf{u}^k + \lambda\Delta\mathbf{u}^k, \quad (25)$$

where the function

$$f(\mathbf{u}^k) = \frac{1}{2}G(\mathbf{u}^k)G(\mathbf{u}^k), \quad (26)$$

is iteratively minimized with respect to λ .

This integrator was implemented using the *PetSc* library [142]. As the dynamics converges towards an attractor an adaptive stepsize control is very efficient. The employed adaptive stepsize control was implemented as described in [143]. The described integration scheme has been generalized for an arbitrary number of real or complex fields. The coupling terms are treated as additional nonlinearities in N . As a common intrinsic timescale we choose $T = tr_z$ with r_z the bifurcation parameter of the OP map. Due to the spatial discretization not all points of the critical circle lie on the grid. Thus, the maximal growth

rate on the discretized circle is not exactly equal to r , the theoretical growth rate. In particular, some modes may be suppressed or even become unstable. Due to this we expect deviations from analytical solutions. To minimize such deviations the size of the critical circle was chosen such that this disbalance between the active modes was minimized. Periodic boundary conditions were applied to account for the translation invariance of the spatial pattern.

Acknowledgments

We thank Ghazaleh Afshar, Eberhard Bodenschatz, Theo Geisel, Min Huang, Wolfgang Keil, Michael Schnabel, Dmitry Tsigankov, and Juan Daniel Flórez Weidinger for discussions.

References

1. Grinwald A, Lieke E, Frostig RD, Gilbert CD, Wiesel TN (1986) Functional architecture of cortex revealed by optical imaging of intrinsic signals. *Nature* 324: 361–364.
2. Blasdel GG, Salama G (1986) Voltage-sensitive dyes reveal a modular organization in monkey striate cortex. *Nature* 321: 579–585.
3. Swindale NV, Matsubara J, Cynader M (1987) Surface organization of orientation and direction selectivity in cat area 18. *J Neurosci* 7: 1414–1427.
4. Bonhoeffer T, Grinwald A (1991) Iso-orientation domains in cat visual cortex are arranged in pinwheel-like patterns. *Nature* 353: 429–431.
5. Bartfeld E, Grinwald A (1992) Relationships between orientation-preference pinwheels, cytochrome oxidase blobs, and ocular-dominance columns in primate striate cortex. *PNAS* 89: 11905–11909.
6. Blasdel GG (1992) Differential imaging of ocular dominance and orientation selectivity in monkey striate cortex. *J Neurosci* 12: 3115–3138.
7. Obermayer K, Blasdel GG (1993) Geometry of orientation and ocular dominance columns in monkey striate cortex. *J Neurosci* 13: 4114–4129.

8. Bonhoeffer T, Grinwald A (1993) The layout of iso-orientation domains in area 18 of cat visual cortex: optical imaging reveals a pinwheel-like organization. *J Neurosci* 13: 4157-80.
9. Weliky M, Bosking WH, Fitzpatrick D (1996) A systematic map of direction preference in primary visual cortex. *Nature* 379: 725-728.
10. Shmuel A, Grinwald A (1996) Functional organization for direction of motion and its relationship to orientation maps in cat area 18. *J Neurosci* 16: 6945-6964.
11. Chapman B, Stryker MP, Bonhoeffer T (1996) Development of orientation preference maps in ferret primary visual cortex. *J Neurosci* 16: 6443-6453.
12. Rao SC, Toth LJ, Sur M (1997) Optically imaged maps of orientation preference in primary visual cortex of cats and ferrets. *J Comp Neurol* 387: 358-370.
13. Bosking WH, Zhang Y, Schofield B, Fitzpatrick D (1997) Orientation selectivity and the arrangement of horizontal connections in tree shrew striate cortex. *J Neurosci* 17: 2112-2127.
14. Das A, Gilbert CD (1997) Distortions of visuotopic map match orientation singularities in primary visual cortex. *Nature* 387: 594-598.
15. Löwel S, Schmidt KE, Kim DS, Wolf F, Hoffsummer F, et al. (1998) The layout of orientation and ocular dominance domains in area 17 of strabismic cats. *Eur J Neurosci* 10: 2629-2643.
16. Issa NP, Trepel C, Stryker MP (2000) Spatial frequency maps in cat visual cortex. *J Neurosci* 15: 8504-8514.
17. White LE, Coppola DM, Fitzpatrick D (2001) The contribution of sensory experience to the maturation of orientation selectivity in ferret visual cortex. *Nature* 411: 1049.
18. Galuske RAW, Schmidt KE, Goebel R, Lomber SG, Payne BR (2002) The role of feedback in shaping neural representations in cat visual cortex. *PNAS* 99: 17083-88.
19. Xu X, Bosking WH, White LE, Fitzpatrick D, Casagrande VA (2005) Functional organization of visual cortex in the prosimian bush baby revealed by optical imaging of intrinsic signals. *J Neurophysiol* 94: 2748-2762.

20. Li Y, Fitzpatrick D, White LE (2006) The development of direction selectivity in ferret visual cortex requires early visual experience. *Nature Neuroscience* 9: 676–681.
21. White LE, Fitzpatrick D (2007) Vision and cortical map development. *Neuron* 56: 327–338.
22. Wolf F, Geisel T (1998) Spontaneous pinwheel annihilation during visual development. *Nature* 395: 73–78.
23. Hoffsummer F, Wolf F, Geisel T, Löwel S, Schmidt KE (1996) Sequential bifurcation and dynamic rearrangement of columnar patterns during cortical development. In: Bower J, editor, *Computation and Neural Systems*.
24. Goodhill GJ, Cimponeriu A (2000) Analysis of the elastic net model applied to the formation of ocular dominance and orientation columns. *Comput Neural Syst* 11: 153–168.
25. Carreira-Perpinan MA, Lister RJ, Goodhill GJ (2005) A computational model for the development of multiple maps in primary visual cortex. *Cereb Cortex* 15: 1222–1233.
26. Yu H, Farley BJ, Jin DZ, Sur M (2005) The coordinated mapping of visual space and response features in visual cortex. *Neuron* 47: 267–280.
27. Erwin E, Obermayer K, Schulten K (1995) Models of orientation and ocular dominance columns in the visual cortex: A critical comparison. *Neural Computation* 7: 425–468.
28. Obermayer K, Blasdel GG, Schulten K (1992) Statistical-mechanical analysis of self-organization and pattern formation during the development of visual maps. *Phys Rev A* 45: 7568–7589.
29. Farley BJ, Yu H, Jin DZ, Sur M (2007) Alteration of visual input results in a coordinated reorganization of multiple visual cortex maps. *J Neurosci* 27: 10299–10310.
30. Swindale NV (2004) How different feature spaces may be represented in cortical maps. *Network: Comput Neural Syst* 15: 217–242.
31. Swindale NV (2000) How many maps are there in visual cortex? *Cereb Cortex* 10: 633–634.
32. Bednar JA, Miikkulainen R (2006) Joint maps for orientation, eye, and direction preference in a self-organizing model of V1. *Neurocomputing* 69: 1272–1276.

33. Cho MW, Kim S (2005) Different ocular dominance map formation influenced by orientation preference columns in visual cortices. *Phys Rev Lett* 94: 068701.
34. Cho MW, Kim S (2004) Understanding visual map formation through vortex dynamics of spin hamiltonian models. *Phys Rev Lett* 92: 018101.
35. Nakagama H, Tani T, Tanaka S (2006) Theoretical and experimental studies of relationship between pinwheel centers and ocular dominance columns in the visual cortex. *Neuroscience Research* 55: 370–382.
36. Erwin E, Miller KD (1998) Correlation-based development of ocularly matched orientation and ocular dominance maps: Determination of required input activities. *J Neurosci* 18: 9870–9895.
37. Pierre DM (1997) Modeling Orientation and Ocular Dominance Columns in the Visual Cortex. Ph.D. thesis, MIT.
38. Grossberg S, Olson SJ (1994) Rules for the cortical map of ocular dominance and orientation columns. *Neural Networks* 7: 883–894.
39. Reichl L, Heide D, Löwel S, Crowley JC, Kaschube M, et al. Coordinated optimization of visual cortical maps (I) Symmetry-based analysis. .
40. Hübener M, Shoham D, Grinwald A, Bonhoeffer T (1997) Spatial relationships among three columnar systems in cat area 17. *J Neurosci* 17: 9270–9284.
41. Engelmann R, Crook JM, Löwel S (2002) Optical imaging of orientation and ocular dominance maps in area 17 of cats with convergent strabismus. *Visual Neuroscience* 19: 39–49.
42. Kaschube M, Schnabel M, Löwel S, Coppola DM, White LE, et al. (2010) Universality in the evolution of orientation columns in the visual cortex. *Science* 330: 1113–1116.
43. Miller KD (2010) π = visual cortex. *Science* 330: 1059–1060.
44. Stevens CF (2011) A universal design principle for visual system pinwheels. *Brain Behav Evol* 77: 132-135.
45. Kaschube M, Wolf F, Geisel T, Löwel S (2002) Genetic influence on quantitative features of neocortical architecture. *J Neurosci* 22: 7206–7217.

46. Kaschube M, Wolf F, Puhlmann M, Rathjen S, Schmidt KE, et al. (2003.) The pattern of ocular dominance columns in cat primary visual cortex: Intra- and interindividual variability of column spacing and its dependence on genetic background. *Eur J Neurosci* 18: 3251–3266.
47. Swindale NV (1982) A model for the formation of orientation columns. *Proc R Soc Lond B* 215: 211–230.
48. Swindale NV (1992) A model for the coordinated development of columnar systems in primate striate cortex. *Biol Cybern* 66: 217–230.
49. Swindale NV (1996) The development of topography in the visual cortex: A review of models. *Network* 7.
50. Ohki K, Chung S, Kara P, Hübener M, Bonhoeffer T, et al. (2006) Highly ordered arrangement of single neurons in orientation pinwheels. *Nature* 442: 925.
51. Obermayer K, Blasdel GG (1997) Singularities in primate orientation maps. *Neural Computation* 9: 555–575.
52. Bonhoeffer T, Kim DS, Malonek D, Shoham D, Grinwald A (1995) Optical imaging of the layout of functional domains in area 17 and across the area 17/18 border in cat visual cortex. *Eur J Neurosci* 7: 1973–1988.
53. Mermin ND (1979) The topological theory of defects in ordered media. *Rev Mod Phys* 51: 591–648.
54. Wolf F, Pawelzik K, Scherf O, Geisel T, Löwel S (2000) How can squint change the spacing of ocular dominance columns? *J Physiol* 94: 525–537.
55. Swift JB, Hohenberg PC (1977) Hydrodynamic fluctuations at the convective instability. *Phys Rev A* 15: 319–328.
56. Cross MC, Hohenberg PC (1993) Pattern formation outside of equilibrium. *Rev Mod Phys* 65: 851–1112.
57. Busse FH (1978) Non-linear properties of thermal convection. *Rep Prog Phys* 41: 1929–1967.

58. Bodenschatz E, Pesch W, Ahlers G (2000) Recent developments in Rayleigh-Bénard convection. *Annu Rev Fluid Mech* 32: 709–778.
59. Soward A (1985) Bifurcation and stability of finite amplitude convection in a rotating layer. *Physica D* 14: 227–241.
60. Zhang W, Vinals J (1997) Pattern formation in weakly damped parametric surface waves. *J Fluid Mech* 336: 301–330.
61. Manneville P (1990) *Dissipative Structures and Weak Turbulence*. Academic Press.
62. Diao Y, Jia W, Swindale NV, Cynader MS (1990) Functional organization of the cortical 17/18 border region in the cat. *Exp Brain Res* 79: 271–282.
63. Blasdel GG, Obermayer K, Kiorpes L (1995) Organization of ocular dominance and orientation columns in the striate cortex of neonatal macaque monkeys. *Visual Neuroscience* 12: 589–603.
64. Schnabel M, Kaschube M, Löwel S, Wolf F (2007) Random waves in the brain: Symmetries and defect generation in the visual cortex. *European Physical Journal* 145.
65. Cross MC, Greenside H (2009) *Pattern Formation and Dynamics in Nonequilibrium Systems*. Cambridge University Press.
66. Lee HY, Yahyanejad M, Kardar M (2003) Symmetry considerations and development of pinwheels in visual maps. *PNAS* 100: 16036–16040.
67. Wolf F (2005) Symmetry breaking and pattern selection in visual cortical development. *Les houches 2003 lecture notes. Methods and Models in neurophysics*. Amsterdam: Elsevier.
68. von der Malsburg C (1973) Self-organization of orientation sensitive cells in the striate cortex. *Kybernetik* 14: 85–100.
69. Ritter H, Schulten K (1988) Convergence properties of kohonen’s topology conserving maps: Fluctuations, stability and dimension selection. *Biol Cybern* 60: 59–71.
70. Miller KD, Keller JB, Stryker MP (1989) Ocular dominance column development: Analysis and simulation. *Science* 245: 605–615.

71. Miller KD (1994) A model for the development of simple cell receptive fields and orientation columns through activity-dependent competition between ON- and OFF-center inputs. *J Neurosci* 14: 409-441.
72. Albus K, Wolf W (1984) Early postnatal development of neuronal function in the kitten's visual cortex: A laminar analysis. *Journal of Physiology* 348: 153-185.
73. Frgnac Y, Imbert M (1984) Development of neuronal selectivity in primary visual cortex of cat. *Physiological Reviews* 64: 325-434.
74. Crair MC, Gillespie DC, Stryker MP (1998) The role of visual experience in the development of columns in cat visual cortex. *Science* 279: 556-570.
75. Antonini A, Stryker MP (1993) Development of individual geniculocortical arbors in cat striate cortex and effects of binocular impulse blockade. *J Neurosci* 13: 3549-3573.
76. Frgnac Y, Shulz D, Thorpe S, Bienenstock E (1988) A cellular analogue of visual cortical plasticity. *Nature* 333: 367-370.
77. Frgnac Y, Shulz D, Thorpe S, Bienenstock E (1992) Cellular analogs of visual cortical epigenesis. I. plasticity of orientation selectivity. *J Neurosci* 12: 1280-1300.
78. Shulz D, Frgnac Y (1992) Cellular analogs of visual cortical epigenesis. II. plasticity of binocular integration. *J Neurosci* 12: 1301-1318.
79. Schuett S, Bonhoeffer T, Hübener M (2001) Pairing-induced changes of orientation maps in cat visual cortex. *Neuron* 32: 325-337.
80. Li Y, Hooser SDV, Mazurek M, White LE, Fitzpatrick D (2008) Experience with moving visual stimuli drives the early development of cortical direction selectivity. *Nature* 456: 952-956.
81. Movshon JA, Van Sluyters RC (1981) Visual neural development. *Annual Review of Psychology* 32: 477-522.
82. Ferster D, Miller KD (2000) Neural mechanisms of orientation selectivity in the visual cortex. *Annual Reviews of Neuroscience* 23: 441-471.

83. Fagiolini M, Katagiri H, Miyamoto H, Mori H, Grant SGN, et al. (2003) Separable features of visual cortical plasticity revealed by n-methyl-d-aspartate receptor 2a signaling. *PNAS* 100: 2854-2859.
84. Blakemore C, Van Sluyters RC (1974) Reversal of the physiological effects of monocular deprivation in kittens: further evidence for a sensitive period. *J Physiol* 237: 195-216.
85. Movshon JA (1976) Reversal of the physiological effects of monocular deprivation in the kitten's visual cortex. *J Physiol* 261: 125-174.
86. Gdecke I, Bonhoeffer T (1996) Development of identical orientation maps for two eyes without common visual experience. *Nature* 379: 251-254.
87. Wiesel TN, Hubel DH (1970) The period of susceptibility to the physiological effects of unilateral eye closure in kittens. *J Physiol* 206: 419-436.
88. und R D Freeman CRO (1980) Profile of the sensitive period for monocular deprivation in kittens. *Experimental Brain Research* 39: 17-21.
89. Jones KR, Spear PD, Tong L (1984) Critical periods for effects of monocular deprivation: differences between striate and extrastriate cortex. *J Neurosci* 4: 2543-2552.
90. Pettigrew JD (1978) The paradox of the critical period for striate cortex. Raven Press, 311-330 pp.
91. Kaschube M, Schnabel M, Wolf F, Löwel S (2009) Inter-areal coordination of columnar architectures during visual cortical development. *PNAS* .
92. Wolf F (2005) Symmetry, multistability and long-range interactions in brain development. *Phys Rev Lett* 95: 208701.
93. Keil W, Schmidt KF, Löwel S, Kaschube M (2010) Reorganization of columnar architecture in the growing visual cortex. *PNAS* 107: 12293-12298.
94. Rochefort NL, Narushima M, Grienberger C, Marandi N, Hill DN, et al. (2011) Development of direction selectivity in mouse cortical neurons. *Neuron* 71: 425-432.

95. Duffy KR, Murphy KM, Jones DG (1998) Analysis of the postnatal growth of visual cortex. *Visual Neuroscience* 15: 831-839.
96. Rathjen S, Engelmann R, Struif S, Kaulisch T, Stiller D, et al. (2003) The growth of cat cerebral cortex in postnatal life: a magnetic resonance imaging study. *Eur J Neurosci* 18: 1797-1806.
97. Villablanca JR, Schmanke TD, Lekht V, Crutcher HA (2000) The growth of the feline brain from late fetal into adult life. i. a morphometric study of the neocortex and white matter. *Brain Research* 122: 11-20.
98. Rathjen S, Schmidt KE, Löwel S (2003) Postnatal growth and column spacing in cat primary visual cortex. *Exp Brain Res* 149: 151-158.
99. Wang BS, Sarnaik R, Cang J (2010) Critical period plasticity matches binocular orientation preference in the visual cortex. *Neuron* 65: 246-256.
100. Sato M, Stryker MP (2008) Distinctive features of adult ocular dominance plasticity. *J Neurosci* 28: 10278-86.
101. Lehmann K, Löwel S (2008) Age-dependent ocular dominance plasticity in adult mice. *PLoS ONE* 3: 3120.
102. Kremer Y, Leger JF, Goodman D, Brette R, Bourdieu L (2011) Late emergence of the vibrissa direction selectivity map in the rat barrel cortex. *J Neurosci* 31: 10689-10700.
103. Boyer D, Vinals J (2002) Grain boundary pinning and glassy dynamics in stripe phases. *Phys Rev E* 65.
104. Koulakov AA, Chklovskii DB (2001) Orientation preference patterns in mammalian visual cortex: A wire length minimization approach. *Neuron* 29: 519-527.
105. Grabska-Barwinska A, von der Malsburg C (2008) Establishment of a scaffold for orientation maps in primary visual cortex of higher mammals. *J Neurosci* 28: 249-257.
106. Huang M (2009) Spatio-Temporal Dynamics of Pattern Formation in the Cerebral Cortex. Ph.D. thesis, Göttingen University.

107. Pomeau Y (1986) Front motion, metastability and subcritical bifurcations in hydrodynamics. *Physica D* 23: 3-11.
108. Malomed BA, Nepomnyashchy AA, Tribelsky MI (1990) Domain boundaries in convection patterns. *Phys Rev A* 42: 7244-7263.
109. Bensimon D, Shraiman B, Croquette V (1988) Nonadiabatic effects in convection. *Phys Rev A* 38: 5461-5464.
110. Boyer D, Vinals J (2002) Weakly nonlinear theory of grain boundary motion in patterns with crystalline symmetry. *Phys Rev Lett* 89: 1-4.
111. Jacobs A (1986) Intrinsic domain-wall pinning and spatial chaos in continuum models of one-dimensionally incommensurate systems. *Phys Rev B* 33: 6340-6345.
112. Coulet P, Elphick C, Repaux D (1987) Nature of spatial chaos. *Phys Rev Lett* 58: 431-434.
113. Argentina M, Coulet P (1998) A generic mechanism for spatiotemporal intermittency. *Physica A* 257: 45-60.
114. Paik SB, Ringach DL (2011) Retinal origin of orientation maps in visual cortex. *Nature Neuroscience* 14: 919-926.
115. Soodak RE (1987) The retinal ganglion cell mosaic defines orientation columns in striate cortex. *PNAS* 84: 3936-3940.
116. Wässle H, Boycott BB, Illing RB (1981) Morphology and mosaic of on- and off-beta cells in the cat retina and some functional considerations. *Proc R Soc Lond* 212: 177-195.
117. Ringach DL (2007) On the origin of the functional architecture of the cortex. *PLoS ONE* 2: 251.
118. Ringach DL (2004) Haphazard wiring of simple receptive fields and orientation columns in visual cortex. *J Neurophysiol* 92: 468-476.
119. Adams DL, Horton JC (2003) Capricious expression of cortical columns in the primate brain. *Nature Neuroscience* 6.
120. Adams DL, Horton JC (2002) Shadows cast by retinal blood vessels mapped in primary visual cortex. *Science* 298: 572-576.

121. Giacomantonio CE, Goodhill GJ (2007) The effect of angioscotomas on map structure in primary visual cortex. *J Neurosci* 27: 4935-4946.
122. Zimmermann W, Seesselberg M, Petruccione F (1993) Effects of disorder in pattern formation. *Phys Rev E* 48: 2699-2703.
123. Zimmermann W, Painter B, Behringer R (1998) Pattern formation in an inhomogeneous environment. *Eur Phys J B* 5: 757-770.
124. Hammele M, Schuler S, Zimmermann W (2006) Effects of parametric disorder on a stationary bifurcation. *Physica D* 218: 139-157.
125. Pomeau Y (1993) Bifurcation in a random environment. *Journal de Physique I* 3: 365-369.
126. HZ Shouval and DG, Jones J, Beckerman M, Cooper L (2000) Structured long-range connections can provide a scaffold for orientation maps. *J Neurosci* 20: 1119-1128.
127. Bartsch AP, Hemmen JL (2001) Combined hebbian development of geniculocortical and lateral connectivity in a model of primary visual cortex. *Cybernetics* 84: 41-55.
128. Bednar JA, Miikkulainen R (2003) Self-organization of spatiotemporal receptive fields and laterally connected direction and orientation maps. *Neurocomputing* 52-54: 473-480.
129. Kaschube M, Schnabel M, Wolf F (2008) Self-organization and the selection of pinwheel density in visual cortical development. *New J Phys* 10: 015009.
130. Reichl L, Löwel S, Wolf F (2009) Pinwheel stabilization by ocular dominance segregation. *Phys Rev Lett* 102: 208101.
131. Bressloff PC, Cowan JD (2002) The visual cortex as a crystal. *Physica D* 173: 226-258.
132. Ernst U, Pawelzik K, Sahar-Pikielny C, Tsodyks MV (2001) Intracortical origin of visual maps. *Nature Neuroscience* 4: 431-436.
133. LeVay S, Stryker MP, Shatz CJ (1978) Ocular dominance columns and their development in layer IV of the cat's visual cortex: A quantitative study. *J Comp Neurol* 179: 223-244.
134. Shatz CJ, Lindström S, Wiesel TN (1977) The distribution of afferents representing the right and left eyes in the cat's visual cortex. *Brain Res* 131: 103-116.

135. Shatz CJ, Stryker MP (1978) Ocular dominance in layer iv of the cat's visual cortex and the effects of monocular deprivation. *J Physiol* 281: 267-283.
136. Löwel S, Singer W (1987) The pattern of ocular dominance columns in flat-mounts of the cat visual cortex. *Exp Brain Res* 68: 661-666.
137. Löwel S, Singer W (1990) Tangential intracortical pathways and the development of iso-orientation bands in cat striate cortex. *Brain Research* 56: 99-106.
138. Johns DC, Marx R, Mains RE, O'Rourke B, Marban E (1999) Inducible genetic suppression of neuronal excitability. *J Neurosci* 19: 1691-1697.
139. Slimko EM, McKinney S, Anderson DJ, Davidson N, Lester HA (2002) Selective electrical silencing of mammalian neurons in vitro by the use of invertebrate ligand-gated chloride channels. *J Neurosci* 22: 7373-7379.
140. Brown PN, Saad Y (1990) Hybrid Krylov methods for nonlinear systems of equations. *J Sci and Stat Comput* 11: 450-481.
141. E DJ, Schnabel RB (1983) *Numerical Methods for Unconstrained Optimization and Nonlinear Equations*. Prentice-Hall.
142. Balay S, Buschelman K, Gropp WD, Kaushik D, Knepley MG, et al. (2001). PETSc Web page. URL <http://www.mcs.anl.gov/petsc/petsc-as/>.
143. Press WH (1992) *Numerical recipes in C: The art of scientific computing*. Cambridge University Press.

List of Figures

- 1 **Swift-Hohenberg equation, A** Cross section through the spectrum $\lambda(k)$ of the Swift-Hohenberg operator Eq. (7), $r = 0.1$. **B** Time evolution of the Power, Eq. (8), for spatial white noise initial conditions. 8

- 2 **Pinwheel annihilation, preservation, and generation** in numerical simulations for different strengths of inter-map coupling ϵ and OD bias γ . Color code of OP map with zero contours of OD map superimposed. **A** $\gamma = 0, \epsilon = 0$ **B** $\gamma = 0, \epsilon = 2000$ **C** and **D** $\gamma = 0.15, \epsilon = 2000$. Initial conditions identical in **A - C**, $r_o = 0.2, r_z = 0.02, T_f = 10^4, k_{c,o} = k_{c,z}$. 11
- 3 **Time evolution of the pinwheel density**, $U = \epsilon |\nabla z \nabla o|^4, r_z = 0.05, r_o = 0.25, \gamma = 0.15$. For each parameter set **A-C** simulations in blue started from an identical set of 20 initial conditions. Red dashed lines: $\rho = 4 \cos(\pi/6)$ and $\rho = 6 \cos(\pi/6)$, black dashed line: $\rho = \pi$. **A** $\epsilon = 0$ **B** $\epsilon = 200$ **C** $\epsilon = 2000$. **D** Normalized power of OP map, $\epsilon = 0$ (red), $\epsilon = 200$ (blue), and $\epsilon = 2000$ (green). In green **C**: OD and OP stripes as initial conditions. Parameters: 128×128 mesh, $\Gamma = 22$ 12
- 4 **Snapshots of the pinwheel crystallization process**. Top panel: OP map, bottom panel: selectivity $|z(\mathbf{x})|$. Left: $T = 0.01$, middle: $T = 0.8$, right: $T = T_f = 10^4$. Parameters as in Fig. 3(c), $\epsilon = 2000, \gamma = 0.15$ 13
- 5 **Distribution of nearest neighbor pinwheel distances during development**. **A-C** rPWC **D-F** hPWC. Distance to the next pinwheel of arbitrary **A,D**, opposite **B,E**, and equal **C,F** topological charge. Parameters as in Fig. 3B. 14
- 6 **Distribution of nearest neighbor distances for final states** ($T = T_f = 10^4$). **A** rPWC, **B** hPWC with pinwheels of equal (red) and opposite (blue) charge. **C** and **D** Illustration of occurring pinwheel distances. Pinwheels are marked with star symbols according to their charge. Units are given in Λ . Parameters as in Fig. 3B. 15
- 7 **Pinwheel annihilation and creation**. **A** Creation (blue) and annihilation (red) rates during time evolution. Fit: $c, a = 0.08/T$ (black line). **B,C** Survival fraction (red) and fraction of preserved pinwheels (blue) compared to the initial time $T^* = 0.01$ **B** and $T^* = 2$ **C**. Parameters as in Fig. 3C. 16
- 8 **Map interactions with detuned wavelengths and OD stripes**. OD stripes interacting with OP columns where $\Lambda_o/\Lambda_z > 1$. **A,B** Illustration of active modes in Fourier space with $k_{c,o} < k_{c,z}$, $\alpha = \arccos k_{c,o}/k_{c,z}$. **C,D** $U = \epsilon |\nabla z \cdot \nabla o|^4, \epsilon = 2000$, **E,F** $U = \tau o^4 |z|^4, \tau = 2000$, **C,E** $\Lambda_o/\Lambda_z = 1.3$, **D,F** $\Lambda_o/\Lambda_z = 2$. Left: initial condition, middle: $T = 1$, right: $T = 5 \cdot 10^4$. Parameters: $r_z = 0.05, r_o = 0.2, \Gamma_z = 20, 256 \times 256$ mesh. Initial condition identical in all simulations. 18

- 9 **Map interactions with detuned wavelength and OD hexagons.** $U = \epsilon |\nabla z \cdot \nabla o|^4$.
A $\Lambda_o/\Lambda_z = 38/41 \approx 0.927$, **B** $\Lambda_o/\Lambda_z = 34/41 \approx 0.829$, **C** $\Lambda_o/\Lambda_z = 26/41 \approx 0.634$, **D**
 $\Lambda_o/\Lambda_z = 24/41 \approx 0.586$, **E** $\Lambda_o/\Lambda_z = 22/41 \approx 0.537$, **F** $\Lambda_o/\Lambda_z = 20/41 \approx 0.488$. **G**
Distribution of nearest neighbor pinwheel distances of arbitrary (Left), opposite (Middle),
and equal (Right) topological charge. Parameters: $\gamma = 0.15, r_z = 0.05, r_o = 0.2, \epsilon =$
 $2000, \Gamma_o = 41, T_f = 10^4$, 256×256 mesh. Initial condition identical in all simulations. . . 19
- 10 **Map interactions in higher feature dimensions. A,B** Map layout by interactions
between three columnar systems $(z(\mathbf{x}), o_1(\mathbf{x}), o_2(\mathbf{x}))$. All maps are mutually coupled.
Superimposed on the OP map there are the borders of two real fields (black, white).
A $r_z = r_{o_1} = r_{o_2} = 0.1$ **B** $r_z = 0.01, r_{o_1} = r_{o_2} = 0.1$. **C,D** Interactions with four
columnar systems $(z(\mathbf{x}), o_1(\mathbf{x}), o_2(\mathbf{x}, t), o_3(\mathbf{x}, t))$. **C** $r_z = r_{o_1} = r_{o_2} = r_{o_3} = 0.1$. **D**
 $r_z = 0.01, r_{o_1} = r_{o_2} = r_{o_3} = 0.1$. Superimposed on the OP map there are the borders
the of three real fields (black, gray, white). Left panel: initial conditions, middle panel:
 $T = 10$, right panel: $T = T_f = 5 \cdot 10^4$. **E** Time evolution of the pinwheel density. Parame-
ters in all simulations: $\epsilon = 2000, \gamma = 0, \Gamma = 22, 128 \times 128$ mesh. 22
- 11 **Distribution of nearest neighbor pinwheel distances in higher feature dimen-**
sions. Distance to the next pinwheel of arbitrary (Left), opposite (Middle), and equal
(Right) topological charge. Parameters as in Fig. 10. **A,B** Map layout by interactions
between three columnar systems $(z(\mathbf{x}), o_1(\mathbf{x}), o_2(\mathbf{x}))$, **A** $r_z = r_{o_1} = r_{o_2} = 0.1$, **B** $r_z =$
 $0.01, r_{o_1} = r_{o_2} = 0.1$. **C,D** Interactions with four columnar systems $(z(\mathbf{x}), o_1(\mathbf{x}), o_2(\mathbf{x}, t), o_3(\mathbf{x}, t))$,
C $r_z = r_{o_1} = r_{o_2} = r_{o_3} = 0.1$, **D** $r_z = 0.01, r_{o_1} = r_{o_2} = r_{o_3} = 0.1$ 23